THE MATERIAL PROPERTIES OF
$CsSnBr_3$ AND CsBr:Sn-1%
AND THEIR POTENTIAL AS
SCINTILLATOR DETECTOR MATERIAL

THESIS

Neal Kleinschmidt, Major, USAF

AFIT/GNE/ENP/10-M05

DEPARTMENT OF THE AIR FORCE
AIR UNIVERSITY

AIR FORCE INSTITUTE OF TECHNOLOGY

Wright-Patterson Air Force Base, Ohio

APPROVED FOR PUBLIC RELEASE; DISTRIBUTION UNLIMITED.

THE MATERIAL PROPERTIES OF CsSnBr$_3$ AND CsBr:Sn-1% AND THEIR

POTENTIAL AS SCINTILLATOR DETECTOR MATERIAL

THESIS

Presented to the Faculty

Department of Engineering Physics

Graduate School of Engineering and Management

Air Force Institute of Technology

Air University

Air Education and Training Command

in Partial Fulfillment of the Requirements for the

Degree of Master of Science in Nuclear Engineering

Neal Kleinschmidt, BS, MS

Major, USAF

March 2010

AFIT/GNE/ENP/10-M05

THE MATERIAL PROPERTIES OF CsSnBr$_3$ AND CsBr:Sn-1% AND THEIR

POTENTIAL AS SCINTILLATOR DETECTOR MATERIAL

Neal Kleinschmidt, BS, MS
Major, USAF

Approved:

//SIGNED//
_____   _____
Capt Benjamin R. Kowash (Chairman)   Date

//SIGNED//
_____   _____
Nancy C. Giles Ph.D. (Member)   Date

//SIGNED//
_____   _____
LTC John W. McClory (Member)   Date

AFIT/GNE/ENP/10-M05

Abstract

The search for superior nuclear radiation detection materials is ongoing. Current scintillator materials using Thallium doped Sodium Iodide or Cesium Iodide are the benchmarks for ease of use and quick identification of isotope species. This research aims to explore Cesium Bromide doped with 1% molar tin (CsBr:Sn-1%) and Cesium Tin Bromide (CsSnBr$_3$) as candidate materials for a new scintillator. The techniques of Extended X-Ray Absorption Fine Structure (EXAFS), X-Ray Absorption Near Edge Structure (XANES) and Cathodoluminescence are used to determine the suitability of CsSnBr$_3$ and CsBr:Sn-1% with Sn^{4+} as a potential scintillator materials and explore their crystal and electronic structures. Comparisons with current published work by Savchyn et al. [2007] on CsSnBr$_3$ and CsBr:Sn-1% with Sn^{2+} will be made. Cathodoluminescence shows the CsBr:Sn-1% with Sn^{4+} to luminesce at 2.4-eV and 3.0-eV, green and violet respectively, indicating the strong possibility of using CsBr:Sn-1% as a scintillator.

Acknowledgements

Table of Contents

List of Figures

List of Tables

THE MATERIAL PROPERTIES OF $CsSnBr_3$ AND CsBr:Sn-1% AND THEIR

POTENTIAL AS SCINTILLATOR DETECTOR MATERIAL

I. Introduction

The search for newer scintillating materials for nuclear detection has been ongoing. This body of research aims to characterize CsBr doped with 1% molar weight Sn and $CsSnBr_3$ as candidate scintillation materials. The luminescent properties of CsBr:Sn-1% and $CsSnBr_3$ has been researched in prior work but has not been characterized as a scintillator material for nuclear radiation detection [Savchyn et al., 2007].

CsBr:Sn-1% is the focus of this study for a couple of reasons. First, like NaI(Tl), it is an alkali halide material lending itself to doping. Second, the probablity of radiation interaction is increased with the high atomic number, or Z number, of the materials composing CsBr:Sn-1% [Turner, 2007]. Scintillator materials such as NaI(Tl) and CsI(Tl) are also high Z crystals. Combining these attributes with the previous cathodoluminescence work by Savchyn et al. [2007] makes CsBr:Sn-1% a good candidate for scintillation study. Savchyn et al. [2007] states these materials luminesce in the red and infrared regions and should be studied for luminescent uses. The work done here will be an extension to research conducted on its crystal structure using the Extended X-ray Absorption Fine Structure (EXAFS) and X-ray Absorption Near Edge Structure (XANES) analysis tecniques.

Several analysis techniques are used to describe crystal structure and their associated electronic structure. EXAFS is the first technique used in this research to describe the crystal structure. Highly accurate measurements of atomic structure can be analyzed using EXAFS. For example, distances between atoms within the crystal

can be measured to within ± 0.5-Å. The Sn dopant in the CsBr:Sn-1% crystal is the main focus of the EXAFS research. The data analysis suggests the Sn to be 3.1$\pm$0.2-Å away from the Cs atoms within the crystal. The Sn is also distributed throughout the crystal. Most CsBr:Sn-1% crystal exhibit a clustering of the tin in microcrystal strucutcures [Savchyn et al., 2007]. A homogenous distribution of the Sn may provide a higher probablity of photon interaction as opposed to the clustered distribution.

Another x-ray absorption structure studied in this work is the XANES structure. XANES data is taken with EXAFS experiments. Both areas are a part of the entire x-ray absorption structure. The XANES structure is used for fingerprinting the oxidation state of Sn within the crystals. Samples of SnO^{+2}, $SnO_2{}^{4+}$ were used to perform this analysis due to their known oxidation states. The analysis shows the Sn within the CsBr:Sn-1% to be in a 4+ oxidation state. The 4+ oxidation state lead into the luminescence part of this study.

Published literature, Savchyn et al. [2007], shows CsBr:Sn-1% with Sn^{2+} to luminesce in the red and infrared when radiated with high energy electrons. Cathodoluminescence was used to produce the Savchyn et al. [2007]data and was repeated for the thesis research on the CsBr:Sn-1% samples containing Sn^{4+}. The data shows a shift of the luminescence to the violet and blue part of the visible spectrum. The shift to violet makes the crystal attractive for common nuclear scintillation applications. Most photomultiplier tubes used in scintillation research are more sensitive to this part of the visible spectrum.

Current luminescence work, other than CL, for CsBr:Sn-1% or $CsSnBr_3$ with Sn^{4+} was not found during the literature review. Current work with CsBr species involves Europium dopants within the matrix [Zorenko et al., 2003]. In the Zorenko et al. [2003] work the CsBr:Eu samples contained a 0.42% mol Eu concentration. A He-

Cd laser with excitation wavelength of $\lambda = 325$-nm was used [Zorenko et al., 2003]. Light Emitting Diodes (LED), in the UV range, were also explored but never used. Other Eu dopant photoluminescence experiments shocased this technique [Weidner et al., 2007]. Photoluminescence experiments using gamma ray sources would be the next step with the CsBr:Sn-1% and CsSnBr$_3$ research. Some photoluminescence work was performed for this research but was not included due to its poor quality. This could be improved by using larger samples of CsBr:Sn-1% and CsSnBr$_3$. The larger crystals could be cut and formed for optical coupling to a PMT. The crystals used in this experiment were 5-mm in diameter or less with very rough surfaces. Thus, optical coupling would be difficult at best.

Impurities were found in the crystals via the EXAFS data. The CsBr:Sn-1% in particular shows a Calcium K-edge implurity located closely to the Sn L-III edge which was the edge of interest. To further characterize the impurities in the CsBr:Sn-1% and CsSnBr$_3$ crystals the X-Ray Fluroescence (XRF) technique was used. Other impurities were found in the both CsBr species. Yet, there is no evidence suggesting these impurities affected the outcome of the cathodoluminescence experiments. The Ca impurity was found in both CsSnBr$_3$ and CsBr:Sn-1% in very small ammounts of approximately 2% or less. In some experiments it was not even found. The XRF data can be found in Appendix F.

There are a few potential benifits to this research. A new crystal with a high resolution is possible. Faster decay times could also be discovered. Both CsBr:Sn-1% and CsSnBr$_3$ could prove to be the next scintillator material of choice. The lifetime of the decay and compton spectrum response need to be measured to draw these conclusions. The research for this thesis aimed, first, to provide information on the luminescent properties of these crystals with Sn in the 4+ state. The second goal was to make a first order assesment on their potential as scintillators.

Both goals were confirmed primarily through cathodoluminescence. The CsBr:Sn-1% crystal is the predominant candidate crystal using cathodoluminescence. The CsSnBr$_3$ crystal produced very little returns. The opaque nature of CsSnBr$_3$ leaves visible light interaction to surface effects at best. A scintillator must be able to pass the light it generates through its volume for registration in a PMT system. The cathodoluminescence results for both crystals clearly suggest CsBr:Sn-1% as a superior scintillator candidate.

II. Crystal Structure and Luminescence Theory

2.1 Extended X-Ray Absorption Fine Structure (EXAFS)

All elements in the periodic table exhibit a characteristic absorption interaction with x-rays and other high energy photons such as gamma rays. When these photons interact with a material a few interaction can occur. The photons can pass through the material without interacting. They can also reflect off the material. Absorption can also occur within the material. Finally, the photons can be attenuated in intensity by absorption and reemission from atoms in the material. The last three interactions reduce the intensity of the original photon stream. This reduction in initial intensity is energy and material dependent. Figure 1 shows the absorption edges of Al, Fe, Sn, Pb, and U from Turner [2007]. These edges occur at the threshold of ionization energy for the respective shells K, L and M, etc.

Material attenuation is the basic principle where EXAFS theory starts. Textbook data commonly shows the linear attenuation coefficient, μ/ρ, for a particular photon or heavy charged particle as shown in Figure 1. The data contains a very fine structure which is described by EXAFS theory. The material attenuation equation is:

$$I = I_o e^{-\mu(E)x}, \tag{2.1}$$

where I is the observed intensity of X-Rays after passing through the material, I_o is the initial intensity, $\mu(E)$ is the material linear absorption coefficient dependent on energy and x is the thickness of the material. Since intensity is a function of energy and the initial energy is known from the synchrotron source, the equation can be solved for $\mu(E)$x and plotted as a function of incoming energy to obtain information found in Figure 2.
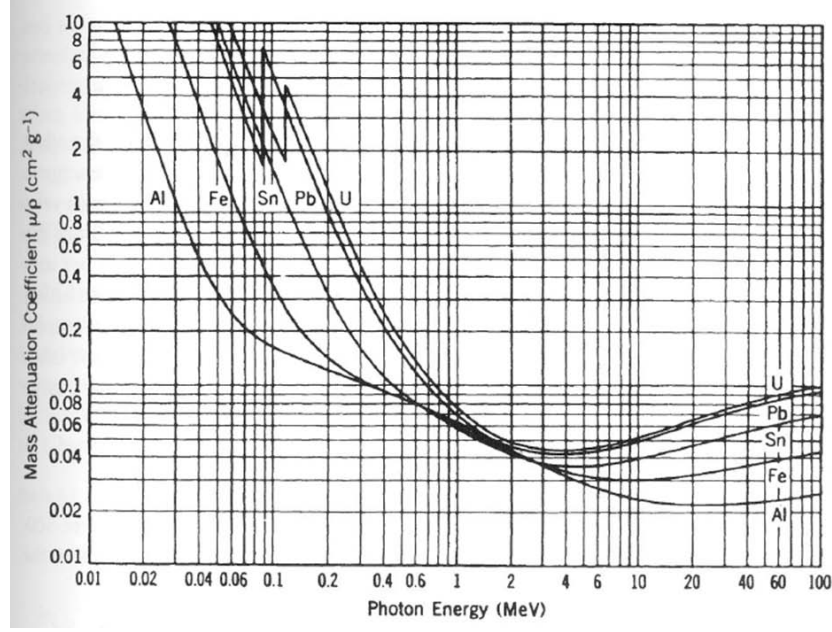
Figure 1. The linear attenuation coefficients of Al, Fe, Sn, Pb, and U are shown here from Turner [2007]. The absorption edges are up in the upper left of the graph where an abrupt stair-like structure is noticed. This is the same structure in Figure 2. The lack of scatter features is noticeable. Figure 2 provides more detail into the fine structure of the crystal.

The EXAFS analysis typically starts at 100-eV to the right of the absorption edge and continues for another 1000-eV. Peaks of the oscillations in the spectrum represent atoms in the crystal. That is, they reveal distances between atoms via scattering. This occurs when the incoming x-ray excites an inner shell electron. In the L-III case this means the $2p_{3/2}$ shell. Figure 3 shows the incoming photon hitting the electron atom/electron complex. The photoelectron propagates through the material running into neighboring atoms and scattering until the photoelectron leaves the material and is measured.

6
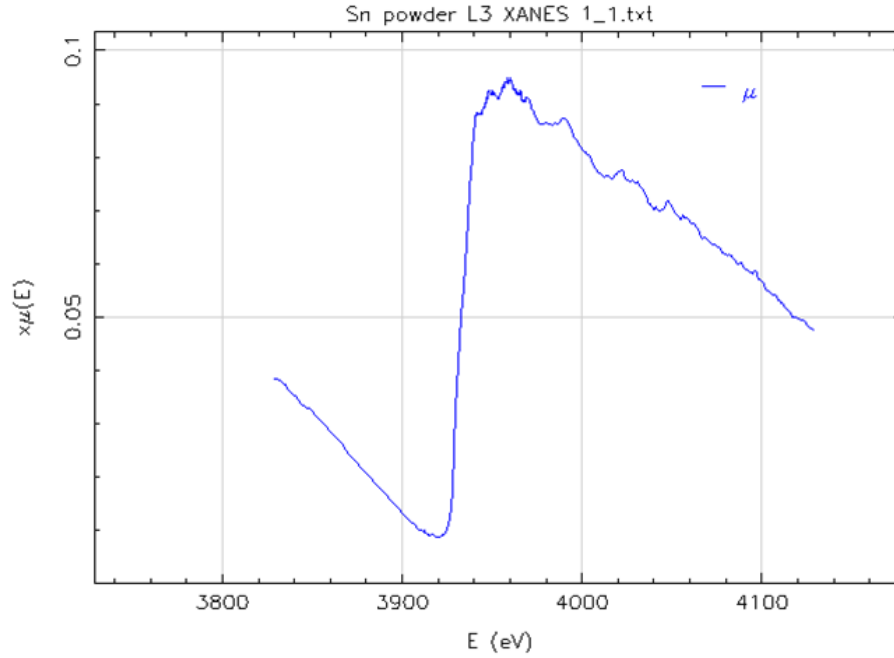
Figure 2. Sn L-III x-ray absorption edge. The plot shows the variation of xμ(E) as a function of x-ray energy-E. This is a very characteristic EXAFS plot and contains much information about the crystal structure and electronic structure within the crystal. The fine structure is more noticeable as compared to Figure 1

.

The process shown in Figure 2 is the result of the photoelectric effect. In the case of Figure 4 an x-ray is used to excite a K shell electron out of its orbit and into the crystal structure. When the electron leaves the atom into the continuum it behaves called a photoelectron and exhibits wavelike properties. These combined physical processes produce the EXAFS and XANES structures.

Some notable features found in Figure 2 need to be discussed. The absorption edge is the most apparent feature. It is the vertical edge. For Sn, the L-III edge happens to be 3929-eV. No matter what material Sn is included in, if the monochromator scans across the L-III edge of Sn this absorption feature will be observed within this area. Thus, the absorption edge is not dependent on the material Sn is included in. This feature gives rise to the ability of material identification based on the EXAFS

7
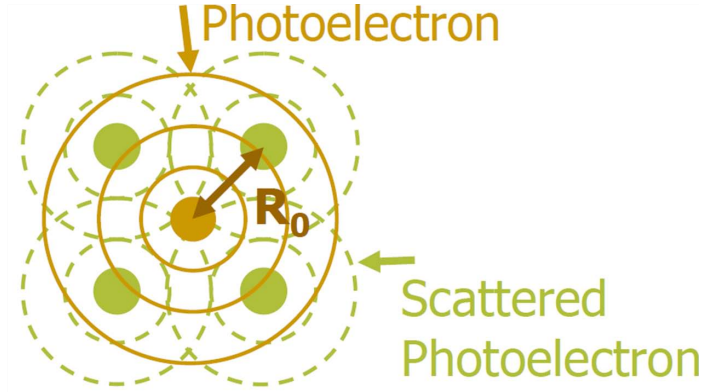
Figure 3. The initial photoelectron is shown as the solid circles traveling from the target atom to the first shell neighbors. The dashed circles are the representation of the scattered photoelectron. These interactions are revealed in the EXAFS data where R_o can be measured [Kelly, 2009a].

structure of a material. There is more spectral variations shown in Figure 2 as compared to Figure 1. These spectral variations are caused by the reflection and scattering of the photoelectron inside of the material before it leaves the material and is measured. An illustration of the scattering and reflection is shown in Figure 3. Other features such as the XANES structure can reveal the electronic structure of the material.

The neighboring atoms scatter in near-symmetry in equidistant shells. The distance to these shells is one of the primary outcomes of EXAFS analysis. The accuracy of these distances can be measured to within ± 0.5-Å revealing a highly accurate structure to the crystal. EXAFS analysis can also be used in amorphous matrices to detect specific bond distances. Doped samples can be analyzed for dopant distribution. This will be performed in this analysis with the CsBr:Sn-1% samples.
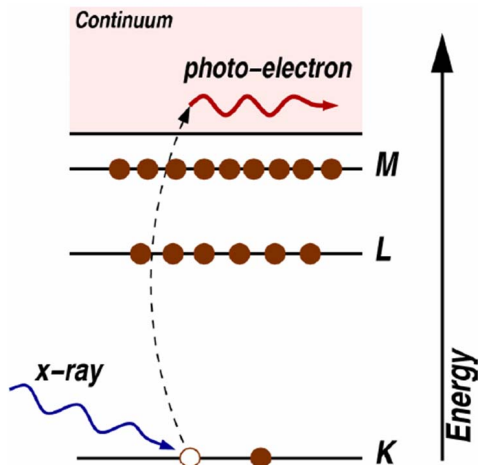
Figure 4. The photo electric effect is the ejection of an inner shell electron. The K-edge electron is shown as the ejected electron here. In the Figure 2 example the L-III electron is ejected from x-ray excitation. The edge feature is caused by the energy requirement to eject the selected electron. In the L-III case of tin, the energy required to do this is 3929-eV. The Figure is from Newville [2004].

The X-Ray Near Edge Absorption Structure (XANES), is the first peak-like structure following the edge structure. If the oxidation state of a truth material is known, the position of the XANES structure can reveal the oxidation state of the same atom species in the material of interest. The truth material can be elemental or a compound. The compounds of SnO^{2+} and SnO_2^{4+} were used in this study. The characteristic absorption edge will always appear in the same area for the atomic species but the XANES can move depending on the oxidation state. The XANES structure shift is due to the change in the Coulomb force. When the oxidation state of an atom is higher, or more positive, the required energy to liberate the inner electron shells, is higher due to the greater attraction of the electrons to the nucleus. Conversely, when the oxidation state is lower, the Coulomb force is more balanced. Less energy is required to achieve excitation when the attractive force is not as great. This phenomena can be seen in Figure 5.

In this example two oxides containing Chromium exhibit the XANES structure at different energies. This is due to the different oxidation state of Cr^{6+} and Cr^{3+}.

9
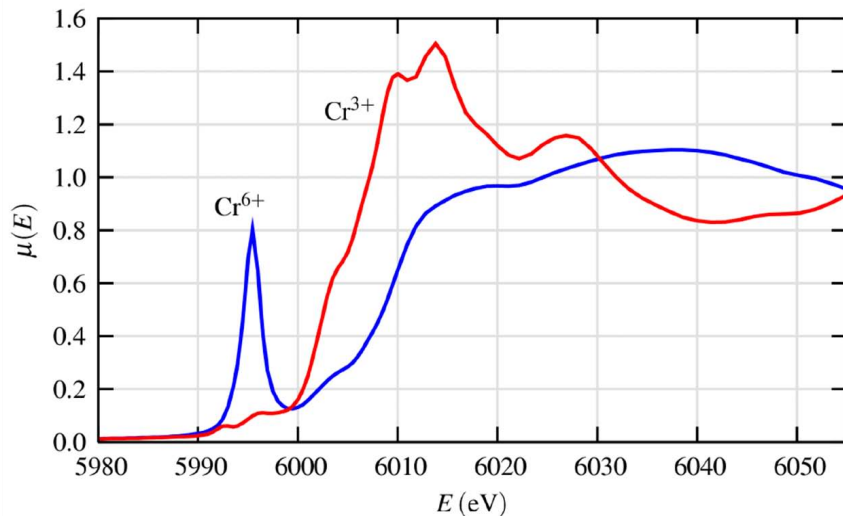
Figure 5. In this Chromium Oxide example the Cr^{3+} XANES structure appears at a different energy than the Cr^{6+} [Newville, 2004].

This attribute will be demonstrated later with the $CsSnBr_3$ and CsBr:Sn-1% data. A similar example to the XANES technique performed in this research deals with Pu contamination at Rocky Flats. Rocky Flats was a Pu processing plant for nuclear weapons until 1989 [Clark, 2002]. Figure 6 shows the XANES analysis performed for the Rocky Flats cleanup.

XANES structures shown in Figure 6 demonstrate the position of XANES is proportional to the oxidation state. Higher oxidation states exhibit higher energy XANES structure peaks. The Pu studies on Rocky Flats led to the appropriate remediation actions based on the Pu interaction with the water tables in the area around Rocky Flats. The data sets ultimately saved taxpayers millions of dollars in unnecessary cleanup actions [Clark, 2002].

The XANES and EXAFS structures are caused by the interference of the scattering atoms in the crystal. If the absorbing atom were isolated the EXAFS the spectrum would look like sharp edge of U in the 1. The real world case presents a different set of data. A presentation of the ideal case is in Figure 7.
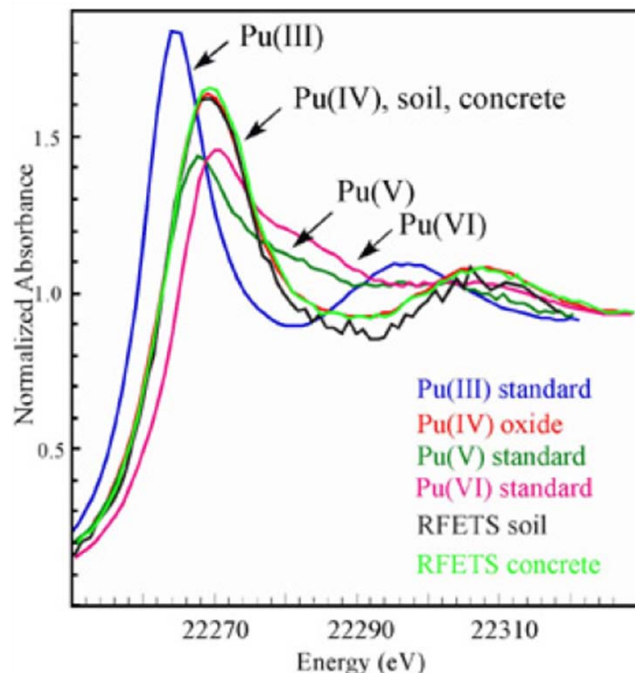
Figure 6. Pu standards in oxidation states of 3+, 4+, 5+ and 6+ were used to identify the Pu pollution in the Rocky Flats area. The identification of the Pu^{4+} oxidation state aided environmental models in determining the area affected by Pu the leaks [Clark, 2002].

The initial interaction of the x-ray is shown coming in from the left. The x axis is the representation of E_o of the target atom. When the energy of the x-ray is sufficient the target electron is boosted to the higher level continuum in the form of a photoelectron. The probability of absorption is shown on the right side of the graph and is the absorption spectra rotated to the vertical. The cross section for absorption increases drastically until the ionization energy is achieved for the target electron orbit. The absorption spectrum is featureless due to the lack of neighboring atoms for the photoelectron to interact with. The EXAFS and XANES structures are caused by the introduction of neighboring atoms in the crystal.

A few interactions can occur when the photoelectron encounters the neighboring atoms in the crystal. The photoelectron can be either absorbed, scattered or reflected. Another case occurs when the photoelectron is first scattered, travels to another

11

X-ray Absorption

photo-electron $\lambda \sim (E - E_0)^{-1/2}$

x-ray

core-level

Absorbing Atom

Energy

E_0

Absorption Probability
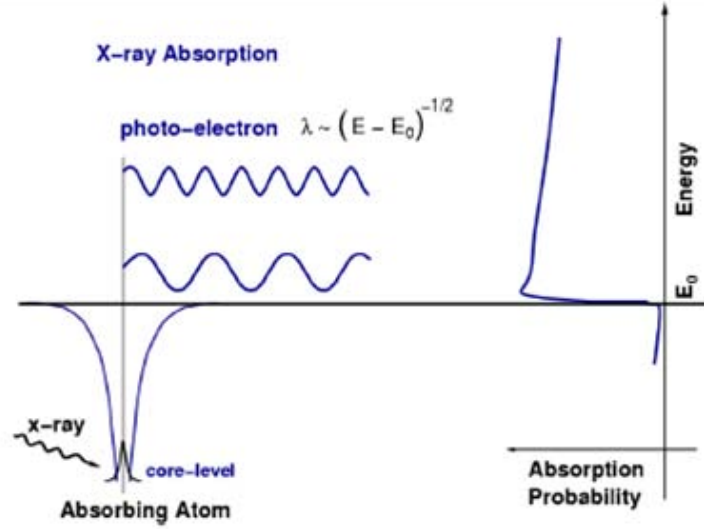
Figure 7. The initial interaction of the x-ray is shown coming in from the left. The x axis is the representation of E_o of the target atom. When the energy of the x-ray is sufficient the target electron is boosted to the higher level continuum in the form of a photoelectron. The probability of absorption is shown on the right side of the graph and is the absorption spectra rotated to the vertical. The cross section for absorption increases drastically until the ionization energy is achieved for the target electron orbit [Newville, 2004].

atom in the crystal and reflects back to the original absorbing atom. Looking at the simple reflection case can explain the EXAFS and XANES structure. When the photoelectron from Figure 7 travels to the first shell neighbor and reflected back to photoelectron wave function is modified in phase and amplitude. Figure 8 depicts this interaction.

The properties of the reflected photoelectron wave are dependent on the reflecting atom [Newville, 2004]. The absorption spectrum shows the constructive and destructive interference of the ideal photoelectron reflection shown in blue. Thus, the spectra following the absorption edge is attenuated causing the XANES and subsequent EXAFS structures at higher energies.
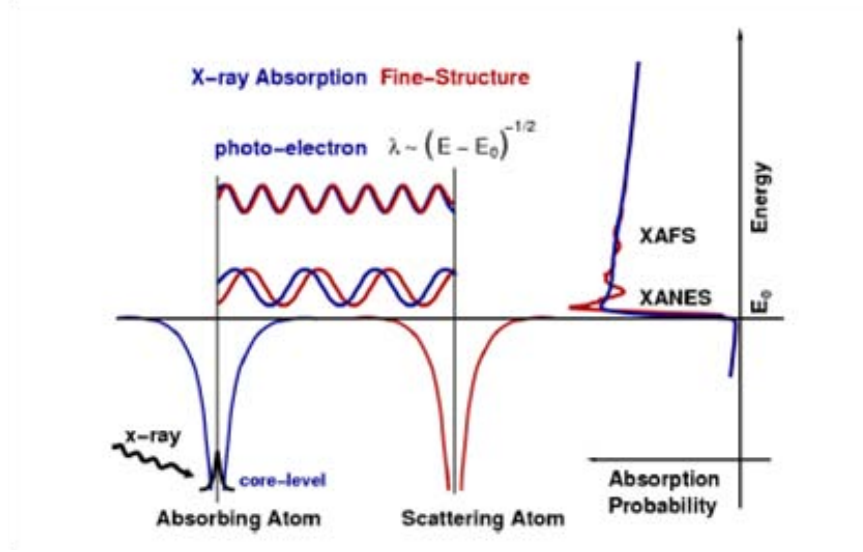
Figure 8. The reflected photoelectron wave representation is shown in the red. The reflecting atom attenuates the photoelectron wave in phase and amplitude. The absorption spectrum shows the constructive and destructive interference of the ideal photoelectron reflection shown in blue. Thus, the spectra following the absorption edge is attenuated causing the XANES and subsequent EXAFS structures at higher energies.

In the case of the CsBr:Sn-1% the published oxidation state of Sn in the CsBr matrix is 2+ [Savchyn et al., 2007]. The XANES analysis will show the Sn samples have an oxidation state of 4+. The published Cathodoluminescence peaks [Savchyn et al., 2007] for CsBr:Sn-1%, Sn^{2+}, are shifted from red and infrared towards the violet blue end of the visible spectrum for the Sn^{4+} samples. Once the raw data is taken and plotted, as in Figure 2, it is normalized to reduce $\mu(E)$ from 0 to 1 to represent the absorption of one x-ray in one atom [Newville, 2004]. This is performed in the calculation

$$\chi(E) = \frac{\mu(E) - \mu_o(E)}{\Delta\mu(E_o)}, \tag{2.2}$$

where $\chi(E)$ term is the normalized oscillatory part of the absorption coefficient μ. $\mu(E)$ is the measured absorption coefficient. The $\mu_o(E)$ term is the theoretical absorption coefficient. It represents the absorption and interaction of one atom isolated

13

from any neighboring atoms. It is the ideal case and is calculated based on a wave equation which represents the photoelectron traveling away from the atom. The denominator term, $\Delta\mu(E_o)$ represents the edge step height. That is, the difference of the pre-edge normalized μ data from the post-edge normalized μ data or basically the height of the step in the staircase.

The data is then converted into k space using

$$k = \sqrt{\frac{2m(E - E_o)}{\hbar^2}}, \tag{2.3}$$

where m is the rest mass of the electron, E is the measured energy and E_o is the ionization energy of the electron level of interest. The data is transformed into k space in order to solve the governing equation of EXAFS analysis which is covered in Appendix A. From k space a Fourier Transform is performed on the data. This puts the data into R space or the radial distribution of the neighboring shells as seen in Figure 3. Spatial analysis can then be performed on the material. This is done by taking the background subtracted EXAFS data, defined by the k and R data, and fitting a pre calculated theoretical model. More detail on this process will be provided after introducing the EXAFS equation.

The k values are then loaded into the EXAFS equation seen below:

$$\chi(k) = \sum_j \frac{N_j e^{-2k^2\sigma_j^2} e^{R_j/\lambda(k)} f_j(k)}{kR^2} \sin[2kR_j + \delta_j(k)], \tag{2.4}$$

where N_j is the number of atoms in the shell, $e^{-2k^2\sigma_j^2}$ is the Debye-Weller term, $e^{R_j/\lambda(k)}$ is the scattering interference reduction term, R_j is the radius of the shell, f_j is the amplitude change of the scattered photoelectron wave function and $\sin[2kR_j + \delta_j(k)]$ is the modulated function of the original scattered electron wave equation ψ. A thorough discussion is found in Appendix A for the derivation of Equation A.1. The

desired end-state is the solutions to the EXAFS equation, A.1, giving the radius to the neighboring atoms, R_o, the change in the half path phase shift, ΔR, the energy shift of the edge, E_o, the mean squared displacement term, σ^2, and the number of atoms in the shell, N [Kelly, 2009b]. Some of these terms are not found in the EXAFS equation but are analogous to the terms within the equation. The R_o is equivalent to the R_j term for one shell. The ΔR is the difference, or uncertainty, of the theoretical model to the measured data. N is usually known from the crystal structure. If N is not known, it can be found by picking the values of the pre-calculated theoretical models and obtaining a good fit to the data. The σ^2 is found in the the Debye-Weller term and is solved for during the comparison to the theoretical values. The E_o value is deduced by running the calculated EXAFS data back through the derivation to Equation 2.2. The theoretical value of E_o, which is actually the starting point of the entire process, is compared to the measured value which would have given the answers to the EXAFS equation. Table 1 lists the acceptable limits for these measurements.

Table 1. Acceptable Thresholds for EXAFS Measurements [Kelly, 2009b].

ΔR	$< 0.5\text{-Å}$
σ^2	$0.003\text{-}0.020\text{-Å}^2$
ΔE_o	$< 10\text{-eV}$

The post processed data is then compared to theoretical calculations of the material structure. These theoretical calculations are possible if the material structure is known or even somewhat known. In the case of this study the material is a crystal with a well known structure.

Most EXAFS analysis can be carried out to the second shell with the $\pm 0.5\text{-Å}$ uncertainty [Als-Nielsen and McMorrow, 2001]. The third shell information is also attainable with extensive data. The structure of most materials can be obtained using a compilation of second shell data of most or all of the atoms in a material. This also

depends on the atom, the electron shell of interest and synchrotron capabilities.

The pre-knowledge of the crystal shape helps in processing EXAFS data. Crystal structures are described by a few methods. The ATOMS program, or web service, uses the space group description of the crystal. First, a crystal space group is chosen. The space group for CsBr:Sn-1% and CsSnBr$_3$ are both of the Pm3m space group. This space group contains assorted cubic structures. The CsBr space group was used to fit the data for the CsBr:Sn-1%. The CsSnBr$_3$ had to be defined based on the known crystal structure provided by [Cole et al., 1990]. Three lengths (a,b and c) are needed for describing the faces of a unit crystal structure. If only one measurement is given, then the other two are equal to this measurement. Three angles are used to describe the angular distribution between the corners of the unit crystal structure. Likewise, if one angle is given, the other two are equal to the first angle. Cubes and other complex structures, for example, can be described in this manner.

Figure 10 shows and example of powder Sn data. The Sn data was used as a truth sample for XANES analysis and also for practice. The lattice constants for Sn in the Beta state (βSn) are a=5.81970-Å, b=5.81970-Å and c=3.1750-Å. The crystal structure of (βSn) is I 41/amd as shown in Figure 9.

The βSn structure gives insight into what is expected in an EXAFS fit. The 3.01617-Å distance described in Figure 9 should be seen as a large peaks in R space. R space is really a magnitude of the Fourier transform outcome. The R function has imaginary parts which are lost during the production of the R space plots. The imaginary and real oscillating functions can be viewed. However, the most meaningful information is found when the magnitude is taken into account. The results are shown in Figure 10 and Table 2. The fit in Figure 10 yield results found in Table 2.
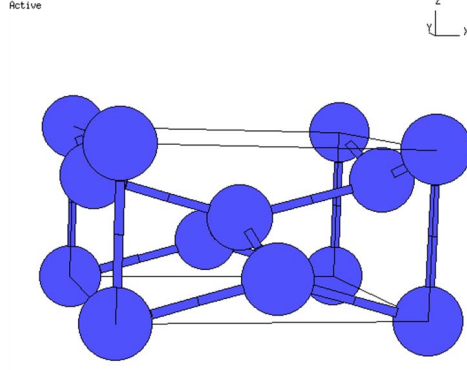
Figure 9. The unit βSn structure shows the Sn atoms throughout the rectangular structure. The lattice constants define the edge lengths of the rectangular parallelepiped shape. The figure shows Sn atoms closer than any of the lattice constants. Thus, the R distance of 3.01617-Å is possible even though it is shorter than any of the lattice constants. Figure adapted from NRL [2004].

Table 2. Results from first shell fits of βSn.

R	3.191867-Å
ΔR	0.175667-Å
σ^2	0.032582-Å^2
$S_o{}^2$	-1.828261
N	4.000000
ΔE_o	3.270141-eV

The CsSnBr$_3$ and CsBr:Sn-1% structures are cubicle as compared to the rectangalloid structure of βSn. The crystal structure of CsBr can be used to describe the CsBr:Sn-1% sample. CsBr is a starting point for the both CsSnBr$_3$ and CsBr:Sn-1%. As the Sn dopant is increased in the CsBr the crystal changes from CsBr:Sn-1% to CsSnBr$_3$. That is, Sn becomes a regular occurrence in the crystal once the concentration of Sn is the same as Cs and becomes CsSnBr$_3$. CsSnBr$_3$ and CsBr are members of the pm3m space group. Although both crystals are part of the pm3m space group their structures are vastly different. CsSnBr$_3$ is part of the E2$_1$ subgroup of pm3m and CsBr:Sn-1% is part of the B2 subgroup. Figures 11 and 12 will show the difference between the two crystals. The position of the Br changes in the lattice as Sn is

'Sn powder L3 XANES 1.txt 2' in R space
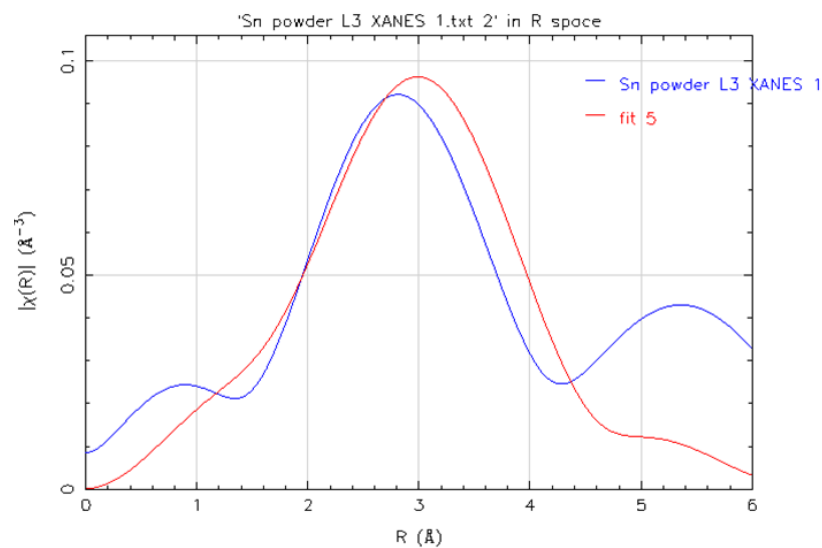
Figure 10. **The first shell of Sn in the β phase is at 3.01617-Å. The data was processed in Athena and then fit using Artemis. The blue line is the processed data and the red line is the first shell fit using the pre-calculated theoretical paths of the photo electron wave traveling to the first neighbor shell and returning back after reflection.**

added. Figure 11 shows the crystal structure of CsBr.
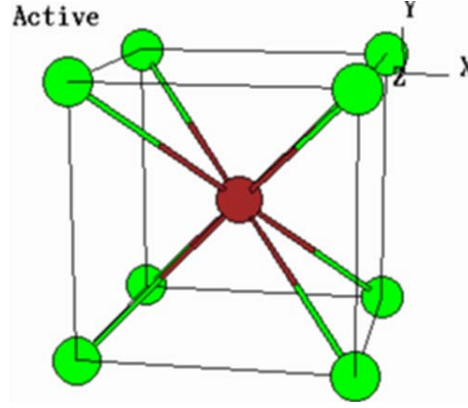
Figure 11. The unit structure of CsBr is shown here. The pm3m structure places either Cs or Br at the center. Cs is chosen for simplicity. To balance CsBr there is one Cs^{1+} for every Br^{1-}. Figure from [NRL, 2004].

The structure of $CsSnBr_3$ places Sn at the center, Cs on the corners and Br on the faces of the cube. The distances between the atoms are different as the lattice constant of CsBr is 4.2953-Å while he lattice constant of $CsSnBr_3$ is 5.8040-Å. Figure 12 shows the structure of $CsSnBr_3$.
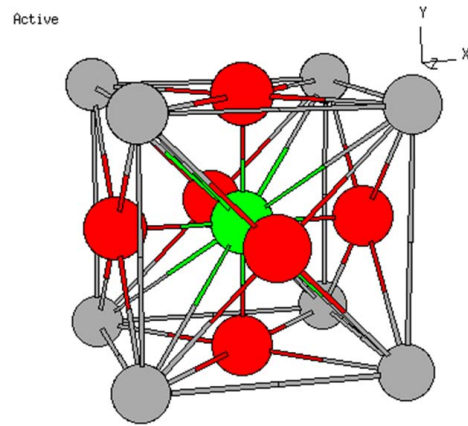
Figure 12. The $CsSnBr_3$ structure is in the same pm3m group as CsBr. The difference is that $CsSnBr_3$ is part of the $E2_1$ subgroup while CsBr is of the B2 subgroup. Here, the grey spheres are the Cs atoms, red spheres are Br atoms and the green sphere is Sn. Figure from [NRL, 2004]

2.2 Cathodoluminescence (CL) Theory

Cathodoluminescence can simulate an environment encountered by scintillating materials. Instead of gamma rays, neutrons or alpha particles the bombarding radiation is a stream of electrons. The excitation is due to the coulomb force interaction of the stream of electrons penetrating the material [Hawkes, 2007]. The incoming electrons excite valence band electrons into the conduction band of the material if the energy threshold for this interaction is met. This energy threshold is usually approximately 3 times the band gap energy [Hawkes, 2007]. Luminescence occurs when the excited electron decays back to another interim state or to its original place. This process is described as the creation of an electron-hole pair [Hawkes, 2007]. When the electron leaves its shell the vacancy left behind can remain empty or be filled with another electron from the continuum or the outer shell of the atom. It is advantageous to nuclear detection if it is visible luminescence. X-rays, Auger-electrons and other electrons are also emitted in the process.

A scintillator works on the same band gap excitation principle [Knoll, 2000]. Certain crystals demonstrate the ability to accept dopant atoms in their structure. In the case of scintillators this provides interim states for electrons to excite to. Figure 13 demonstrates this principle.
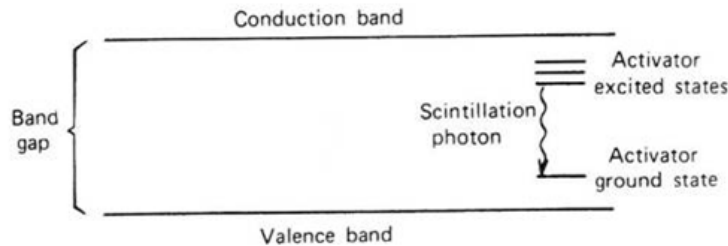
Figure 13. In most scintillator materials the energy band gap makes the probability too low for nuclear radiation to excite an electron to the conduction band. A dopant is added to insert more options for the electron to occupy. These transition levels can also be a ladder to the conduction band but this is not necessary for scintillation luminescence as the picture demonstrates. Thallium doped Sodium Iodide is a good example and is a widely used material. [Knoll, 2000]

20

CL is the primary tool for revealing the luminescence properties of the CsBr crystal species in this study. The published luminosity curves for CL show peaks of luminosity for $CsSnBr_3$ and CsBr:Sn-1% to range in the red and infrared at room temperature [Savchyn et al., 2007]. Figure 14 shows the published data [Savchyn et al., 2007].
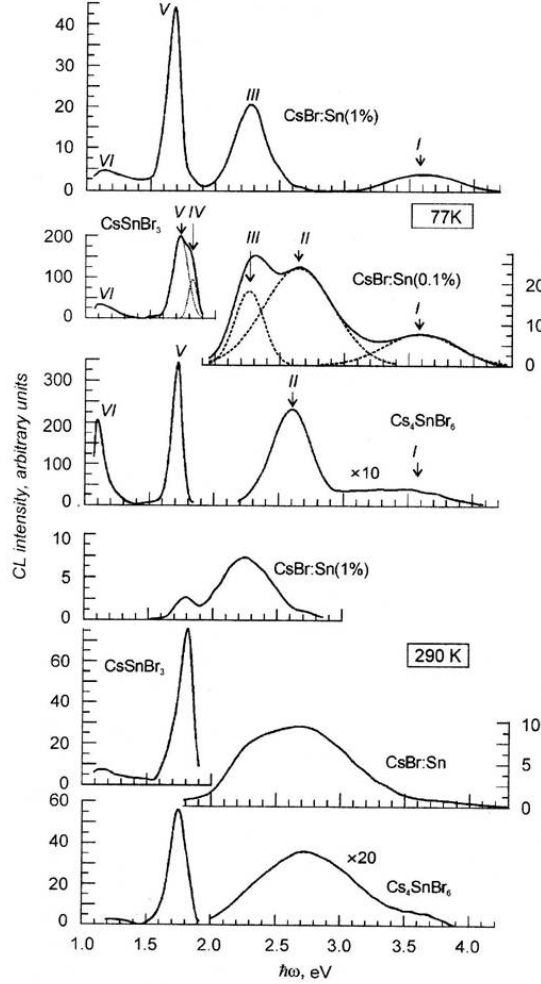
Figure 14. This thesis is aimed at comparing the data at 290K. The equipment setup limited the experiment to room temperature. The figure data shows a response at 2.25-eV for CsBr:Sn-1% which is in the yellow to green region. The $CsSnBr_3$ shows a peak around 1.75-eV which is around the red region [Savchyn et al., 2007].

The data taken for this thesis occurred around 290K, or room temperature [Savchyn et al., 2007]. The lower three graphs of Figure 14 are at the 290K temperature [Savchyn et al., 2007]. Of more particular interest are the graphs for $CsSnBr_3$ and CsBr:Sn-1%. The $CsSnBr_3$ exhibits a peak around 1.75-eV which is 709-nm in the red portion of the visible spectrum. CsBr:Sn-1% exhibits a small peak in the same area. CsBr:Sn-1% has a more intense peak at 2.25-eV. This falls into the yellow to green portion of the visible spectrum. The intensity is different for each crystal. The $CsSnBr_3$ 1.75-eV peak is at 75 intensity units while the CsBr:Sn-1% peak is at 7-8 intensity units. This suggests that $CsSnBr_3$ may be a superior choice if intensity is the most important attribute for scintillation.

The red luminescence of the $CsSnBr_3$ crystal makes it an attractive option for scintillating material [Savchyn et al., 2007]. However, the green emission of the CsBr:Sn-1% crystal may be of interest also. The fact the Sn is in the different valence, 4+ vs. 2+, makes the research novel. A literature search has shown luminescence and crystal structure studies on CsBr species with Sn^{4+} have not been done before.

III. Experimental Setups

3.1 EXAFS

The synchrotron produces electromagnetic radiation in the ultraviolet to the infrared portions of the spectrum. The Double Crystal Monochromator (DCM) line at CAMD utilizes the X-Ray portion, 1-keV to 12-keV, of the synchrotron radiation [CAMD, 2008]. Figure 15 shows most of the tuning equipment for the DCM line.

Figure 15. The DCM line is the x-ray line used for EXAFS, XANES and other x-ray absorption analysis techniques. The double monochromator can be seen on the right side of the image. X-rays exit the synchrotron at various wavelengths. A monochromator is used to tune the x-rays to the desired energy, or I_o. The entire line is kept under vacuum to reduce x-ray interactions with air or other molecules before they hit the samples. The tin foil is used to retain heat during beam line "baking". The separate lines at CAMD are baked intermittently to help release molecules that build up in the lines. Any liberated molecules are quickly expelled in the vacuum process.

The schematic in Figure 16 shows a clearer depiction of the beam line setup. The x-rays travel from left to right in Figure 16. The two gates are used for safety. They are shut when the DCM line is not in use and during experiment setup. This reduces the exposure to the experimenters. The beam line and experiment hutch are surrounded by lead-lined walls. Any glass used between radiation areas and personnel areas also contain lead.

23
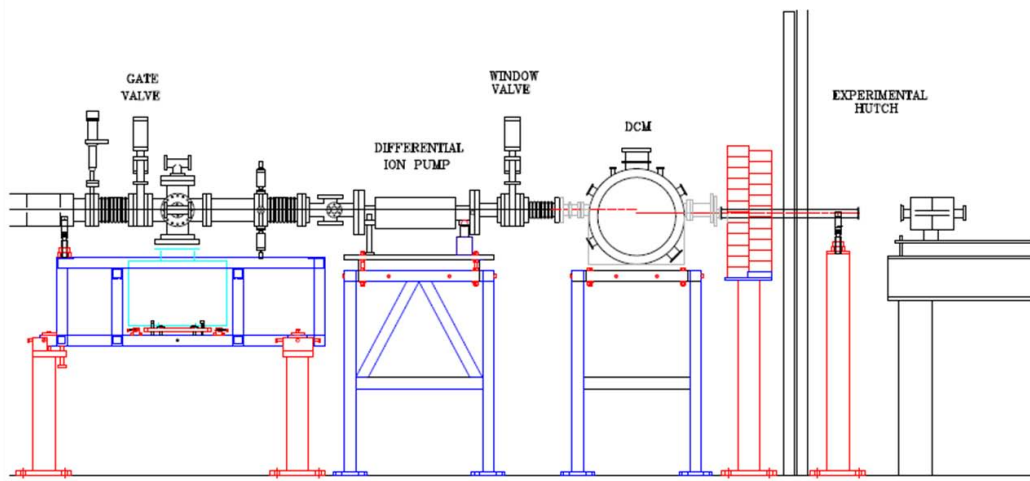
Figure 16. The schematic of the DCM line shows a couple of gates used for safety. The double chromatic monochromator tunes the x-ray to the desired energy.

After I_o is measured in a helium chamber the X-Rays are free to interact with the sample in the experiment hutch. A Canberra 13 element High Purity Germanium (HPGe) diode array detector is used to read the photoelectrons as they leave the sample with the absorption structure information in the form of attenuated energy [CAMD, 2008]. Figure 17 shows the setup of the incoming beam line, sample holder and HPGe instrumentation.

The data taken for this thesis was not obtained during the time of these pictures. The procedures for executing an experiment are as follows. First, a sample is mounted on mylar tape. The mount is then placed in the beam line path while the beam line is shut off. A couple of safety measures are in place to ensure personnel are not exposed to the beam line when it is operational. Dosimeters are worn at all times while in the synchrotron facility. After all safety precaution measures have been accomplished a data run can commence. A DCM specialist usually aids in all of these procedures. The DCM specialist will then set up the computer acquisition system according to experimental parameters. These parameters include beginning and ending energy selection, integration time of the HPGe detector and energy step size. An acquisition

24
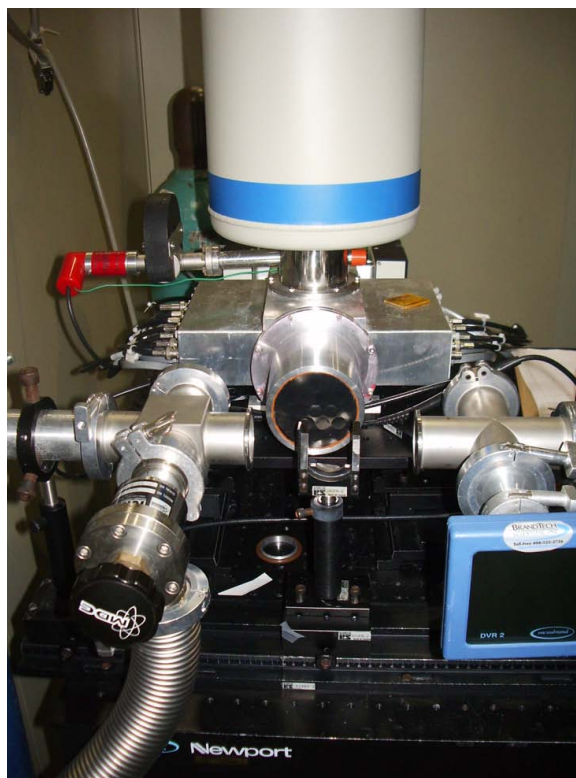
Figure 17. The High Purity Germanium (HPGe) detector is seen behind the sample holder. The x-ray beam comes in from the left. The HPGe detector is multichannel and tuned for specific energies.

cycle can typically take 60-90 minutes depending on the selected parameters. Once a run is complete the data is ready to process.

The data analysis is done on a number of software packages. The software package used for this thesis include Artemis, Athena and Hephaestus [Ravel and Newville, 2005]. Artemis and Athena are based on a legacy code written in Fortran called FEFF [Rehr and Albers, 2000]. FEFF is still in use. Artemis and Athena are a GUI interface to the FEFF program. FEFF involves changing crystal theoretical physical parameters to produce multiple scattering paths based on the crystal structure. Key EXAFS values, as described in the EXAFS theory section, can then be solved for based on theoretical calculations of these multiple scattering paths. Appendix B includes a more thorough discussion of how data is processed in these programs.

3.2 Cathodoluminescence Equipment

Cathodoluminescence is usually performed with a Scanning Electron Microscope (SEM) [Hawkes, 2007]. It can also be performed using a Cathode Ray Tube (CRT) [Ozawa, 1990]. However, highly magnified images, up to 500,000 times, are available via the SEM. The electron energy and current can also be changed quicker with an SEM. The SEM at AFIT is located in the clean room of building 644. CL is used for studying semi-conductors, scintillation material and phosphor screens [Ozawa, 1990]. Figure 18 shows the SEM and attached CL instrument setup.

Figure 18. The SEM is capable of providing 500,000 times magnification for sample imaging. The CL apparatus is on the left side of the image labeled monoCL made by Gatan. A set of computers to the right of the instrument run the SEM and the Gatan CL instrument separately.

The SEM at AFIT is only capable of room temperature measurements. Room temperature in the clean room is ≈71°F. The Savchyn et al. [2007] data was taken at 290K, approximately room temperature, and 77K which is liquid nitrogen temperature. Since cryogenic cooling would not be assumed for a future CsBr:Sn-1% instrument for this thesis, room temperature was adequate for data acquisition. The procedures were simplified and the data requirement was reduced.

The procedures for executing an experiment using the SEM/CL instruments are as follows. First the sample is mounted on a sample pedestal with carbon based tape as seen in Figure 19. The sample must be less than 1-mm in height. Otherwise the CL mirror will be damaged when it is used. The pedstool seen in Figure 19 fits into a mount inside the SEM. The mount can be moved to a desired location and orientation for imaging with the SEM and analysis with the CL instrumentation.

Figure 19. The sample size for the SEM must be less than 1-mm in height. It also cannot go over the edges of the pedestal as seen here. The carbon tape is used to keep the samples from moving during the vacuum process. A pen is included in the picture for scale.

The carbon tape is very sticky to keep samples from moving during the vacuum processes or an accidental tip over of the pedestal during insertion or removal from the SEM. Removing the crystal samples from the carbon tape sometimes pulverized them. If this occurs the mess needs to be cleaned up due to the clean room environment.

Figure 20. The sample exchange chamber is where a vacuum is drawn on the sample and then inserted into the SEM chamber via the pushrod seen protruding from the chamber. The sample pedestal is seen in the foreground with a measuring standard. The entire height of the sample and pedestal must be less than 1-inch to fit under the monoCL mirror for CL analysis. Otherwise, damage can occur to the mirror when it is brought into position for analysis.

Next, the pedestal is screwed on to the sample placement rod and drawn into the sample exchange chamber as seen in Figure 21. The exchange chamber slides up against the SEM vacuum chamber. The exchange chamber is then evacuated equivalent to the vacuum of the SEM. Vacuum pressures are necessary to reduce electron interaction with atoms in the atmosphere.
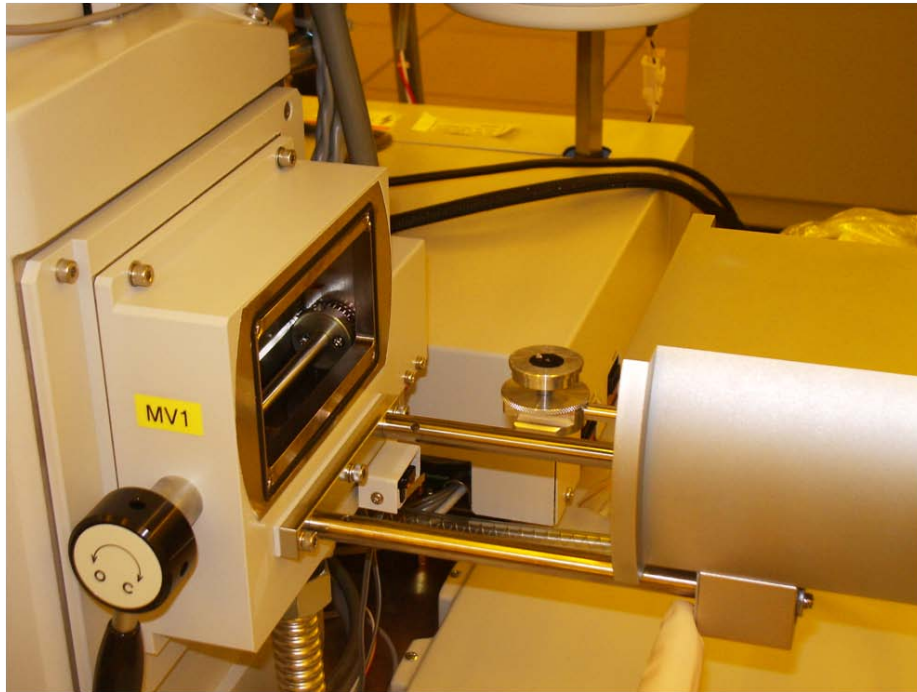
Figure 21. The pedestal is screwed onto the pushrod. The pushrod is then pulled back into the exchange chamber. The knob below the MV1 sticker opens the door between the SEM and sample exchange chambers. The door can only be opened when a vacuum is pulled on the sample exchange chamber. After the sample is pulled back into the exchange chamber, the exchange chamber is pushed against the SEM and the vacuum is pulled.

Next, a door between the sample exchange chamber and the SEM chamber is opened and the sample pedestal is pushed into a mount located below the area where SEM beam will be active. Once the placement rod is removed the door between the sample exchange chamber and the SEM chamber is closed. The high voltage can then be turned on to begin SEM imaging and CL analysis.

After the pedestal mounted in the SEM, imaging of the samples can begin. To get a really good focus it is best to focus at the highest magnification. This is done so that the sample is in focus at lower magnification levels. A good focus is needed to determine which parts of the crystal are being illuminated during CL analysis. A software package controls pedestal position and the imaging specifications for the SEM. The detailed procedures will not be provided here. A lab technician must train and certify a user before they are allowed to use the SEM machine. This is also needed for the CL instrument which is run off a separate computer system. A few images were acquired using the SEM but not used for analysis. They are provided here as a sense of microscopic material characteristics.
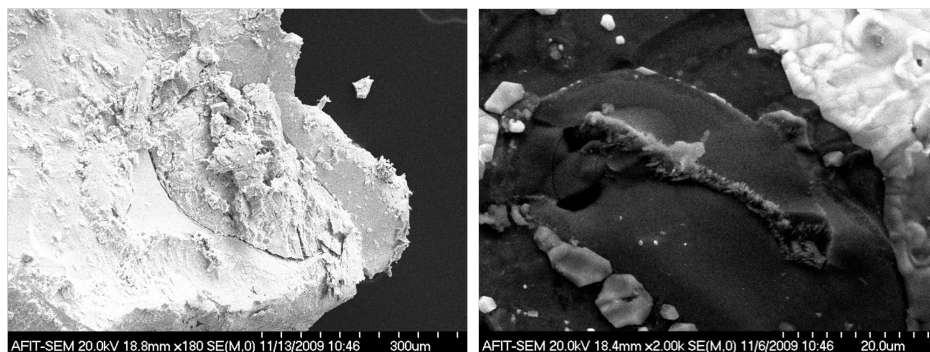
Figure 22. The CsBr:Sn-1% sample is shown close up. The first notable feature is the fleck of The CsBr:Sn-1% to the upper right. Both CsBr:Sn-1% and CsSnBr$_3$ are both brittle. The surface is rough for both samples, as also seen in the right figure. The CsBr:Sn-1% seems to luminesce very brightly under the SEM conditions shown here.

Once the SEM images have been acquired the CL analysis can be executed. CL analysis is performed via the Gatan monoCL instrument attached to the SEM. A different software package controls the CCD data acquisition. The CCD is Si based and has a response between 380-900-nm. Calibration is performed with a well characterized visible light lamp. The instrument can be calibrated with other wavelength sources but they are not available. The data produced is intensity in counts versus wavelength in 0.22-nm intervals. The data must be converted by the user if energy units are desired instead of wavelength. Appendix D covers this process. The integration time and number of frames can be changed in the software.

The experiments executed for this thesis were primarily done in the 380-620-nm range. This was done as there was very little response from the crystals past 620-nm. All data runs were summed frames of 100 second integrations over three frames. That is, each data run took 300 seconds, or five minutes. This integration scheme was found to be optimal to get the sharpest peak data for the shortest ammount of time. An example of a data frame can be seen in Figure 23.
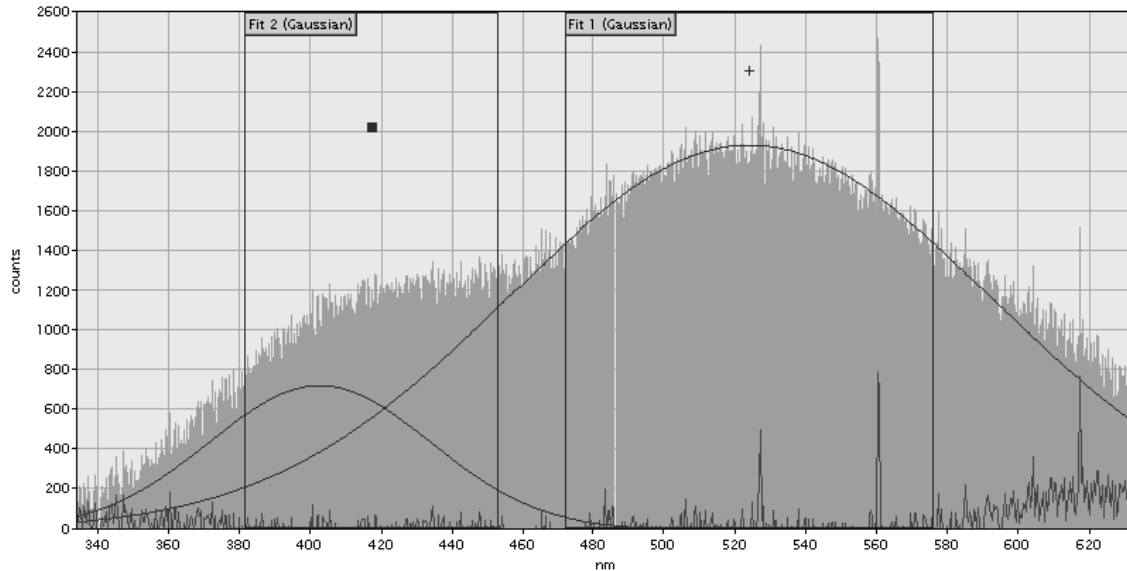
Figure 23. In this image the raw data counts are shown with two regions of interest (ROI). Gaussian fits put the peaks at 402-nm (3.1-eV) and 523-nm (2.4-eV).

31

The software analysis package includes some features such as the Gaussian fitting routine. An ROI must be defined around the peak of interest. The data shown in Figure 23 has a double peak according to the Gaussian fitting routine. As mentioned in the CL theory section these wavelengths translate to 3.0-eV and 2.4-eV, or the violet and green parts of the visible spectrum. The Gatan monoCl SP software also computes the intensities as a function of energy in electron volts. A MATLAB code was used to mesh two separate spectrums for a range of 1.6-eV to 3.5-eV. A MATLAB routine was also written to find the energy peaks as an exercise in converting intensity as a function of wavelength to intensity vs. energy. This is done employing Equation 6.4 found in Appendix D. In order to perform this, the data needs to be saved in the program as a text file. It can then be read into MATLAB and analyzed according to any numerical analysis routine desired by the experimenter.

The equipment details for the SEM and the monoCL instrument can be found in Table 3. Specialized training from a laboratory technician is required for both instruments. Training is also needed for building 644 and clean room access.

Table 3. Cathodoluminescence Equipment.

Equipment	Model	Serial Number
Hitachi SEM	S-4700	6063
Gatan monoCL	7343-0001	2804040001

IV. Results and Analysis

4.1 EXAFS and XANES Results

The ease of fitting EXAFS data depends on a few factors. The first factor is the cleanliness of the data. If the data is noisy it will be difficult to get a good fit in the R space. Smooth k space, and E space data prior to K, means smoother R space data via the Fourier transform. Second, the length of the data after the absorption edge determines how much information is obtainable from the data. EXAFS can extend to 1000-eV after the absorption edge [Kelly, 2009b]. In the case of the data presented here, a 200-300-eV extension is available. The data still produced enough information for first and second shell fits.

The analysis for the EXAFS data included the Cs centered and Sn centered data for both $CsSnBr_3$ and CsBr:Sn-1%. With these data sets the structure of the crystals can be found. $CsSnBr_3$ was used as a reference crystal, due to its well known structure, for finding the structure of the CsBr:Sn-1% in this analysis. The main focus of the analysis was to find the position of the Sn using the EXAFS data and the charge of the Sn using XANES analysis for the CsBr:Sn-1% crystal.

The $CsSnBr_3$ data was fit first. Procedures for EXAFS and XANES data fitting are found in Appendix B. Figure 24 shows the R space fitting of the Cs centered $CsSnBr_3$ data. Tables 4 and 5 are the numerical results of the fitting.

'CsSnBr Cs L3 XANES 1.txt 2' in R space
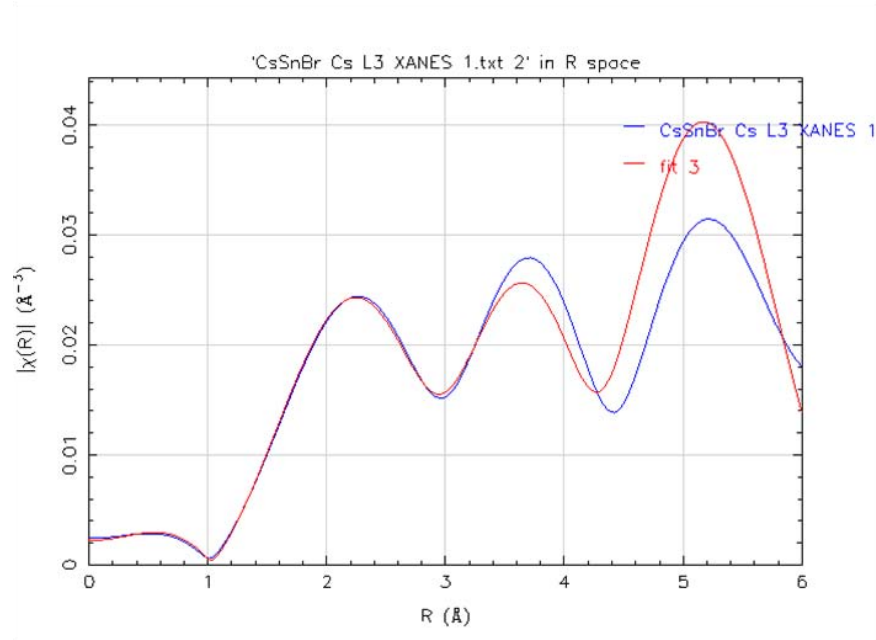
Figure 24. The second peak of this fit is the first shell neighbor of Br atoms at 4.1-Å. Sn second shell neighbors at the third peak at 5.0-Å. The first peak is a half path interference of the Sn shell.

Table 4. Results from first shell fits of CsSnBr$_3$ Cs centered. The first shell is Br Atoms

R	4.02-Å
ΔR	-0.08-Å
σ^2	0.033-Å^2
N	12
ΔE_o	10.1-eV

Table 5. Results from Second shell fits of CsSnBr$_3$ Cs centered. The second shell is Sn Atoms

R	4.94-Å
ΔR	-0.08-Å
σ^2	0.033-Å^2
N	8
ΔE_o	10.1-eV

The values reported in EXAFS analysis are the closest fit to theoretical calculations. Table 4 shows that the first shell R position according to the data is at 4.02-Å. The accepted value is 4.1-Å. Thus, the ΔR reflects the displacement of the data from theory. The σ^2 value is the relative disorder of the crystal due to atomic vibration. The value for σ^2 of 0.033-Å^2 is a little over the maximum acceptable value for σ^2 or 0.02-Å^2. The ΔE_o of 10.1-eV is also just outside the acceptable limit of 10-eV. The out of range values of σ^2 and ΔE_o suggest a better fit could be obtained. Many attempts were tried while constraining some values such as σ^2. These values were constrained to within the acceptable limits to get a better and quicker determination of the R and ΔR functions. This approach was taken due to the focus on the position of the atoms rather than their properties of vibration and overall absorption energy shift. Finding the Sn position in the CsBr:Sn-1% is the most important part of this analysis. Having good position data on the CsSnBr$_3$ crystal will be a good place to start.

The Sn centered data for $CsSnBr_3$ is shown next. The Sn data was noisier than the Cs data for both crystals. A good explanation for this is not available. After processing, the Sn data produced some results which later led to the idea of where the Sn was in the CsBr:Sn-1% crystal. Figure 25 shows the best fit for Sn.
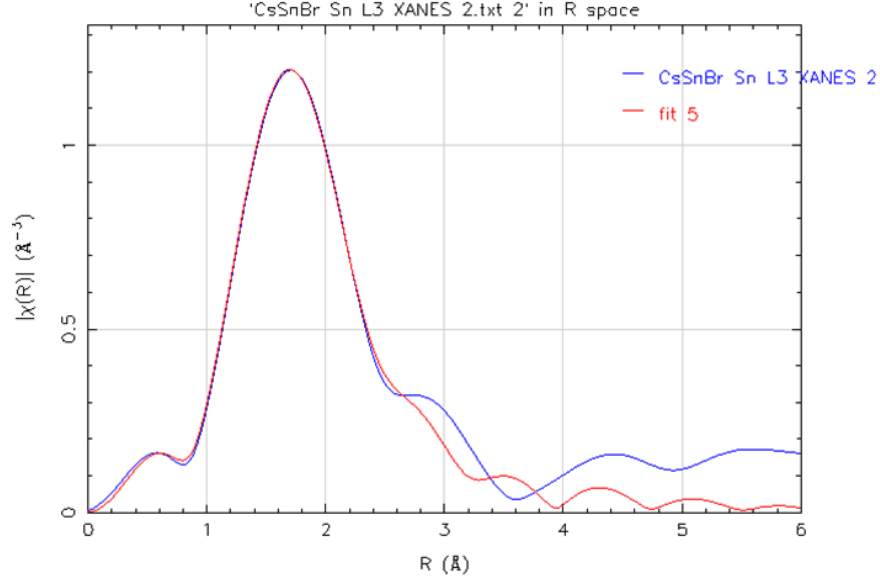
Figure 25. The numerical results for the Sn centered fit in Table 6 are outside of the threshold values typically acceptable for EXAFS data as listed in Table 1.

Table 6. Results from 1st shell fits of $CsSnBr_3$ Sn centered. The first shell is Br Atoms

R	2.1-Å
ΔR	-0.81-Å
σ^2	1.9-Å^2
N	6
ΔE_o	-1.3-eV

The Sn centered data for $CsSnBr_3$ shows an out of range value of -0.81-Å for ΔR. Although it was important to fit the data for R accurately, this was the best fit achieved. However, the data still offered clues to the structure of CsBr:Sn-1%. The Sn fits in the CsBr is actually closer to the accepted value of 2.9-Å of $CsSnBr_3$.

In Figures 5 and 25 the first shell neighbors are Br atoms. The Br atoms are the closest atoms to both Sn and Cs. A structure of the crystal can be deduced from these relative positions. The Sn second shell available in the Cs centered data confirms the well known structure of the $CsSnBr_3$ crystal. The $CsSnBr_3$ Cs and Sn fits were used to see if there were any similarities to the CsBr:Sn-1% structure. The rationale is that the base crystal is CsBr where Sn is progressively added in molecular weight percentage until its concentration matches Cs ultimately producing $CsSnBr_3$. That is, there is a transition from CsBr to CsBr:Sn-1% to $CsSnBr_3$ as Sn is added to the crystal as a dopant. A plot of several Sn centered CsBr:Sn-1% spectra on top of a Sn centered $CsSnBr_3$ spectrum was made to see if any similarities exist. This can be seen in Figure 26.
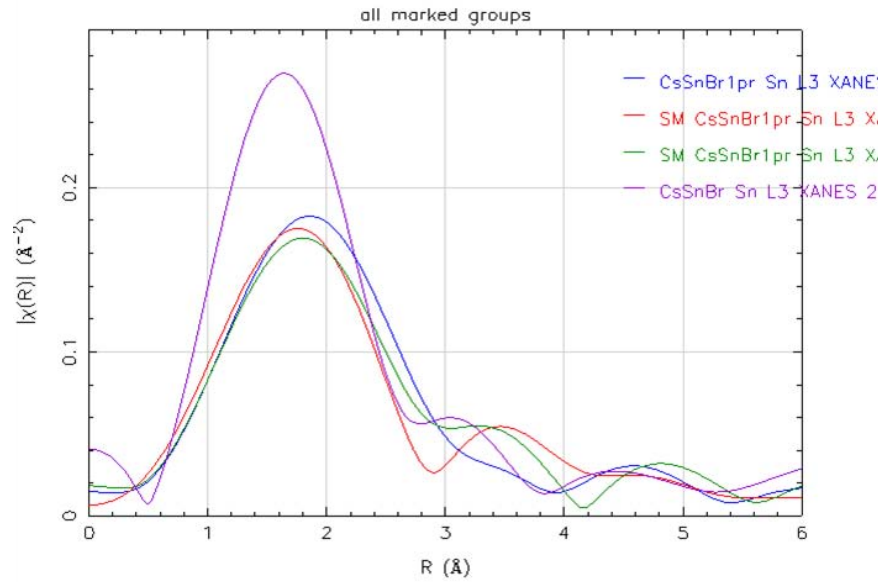
Figure 26. The $CsSnBr_3$, Sn centered, plot is show in purple. The other plots are Sn centered CsBr:Sn-1%. In all cases the distance to the Br peak is shown. There is a little difference in the position of the Br shell between $CsSnBr_3$ and CsBr:Sn-1%.

The close values of the Br peaks when $CsSnBr_3$ and CsBr:Sn-1% are compared for Sn centered data show the similarity of the distance between Sn and Br. The Sn-Br distance in CsBr:Sn-1% is a little larger by inspection. The first shell of Br is

at 4.1-Å in $CsSnBr_3$ as shown by the red line in Figure 27. The second shell made up of Sn is at 5.0-Å. The blue line represents the CsBr:Sn-1% data. The first shell of Br in both cases are pretty close. However, the CsBr:Sn-1% is missing the second shell of Sn. Figure 27 will show this.
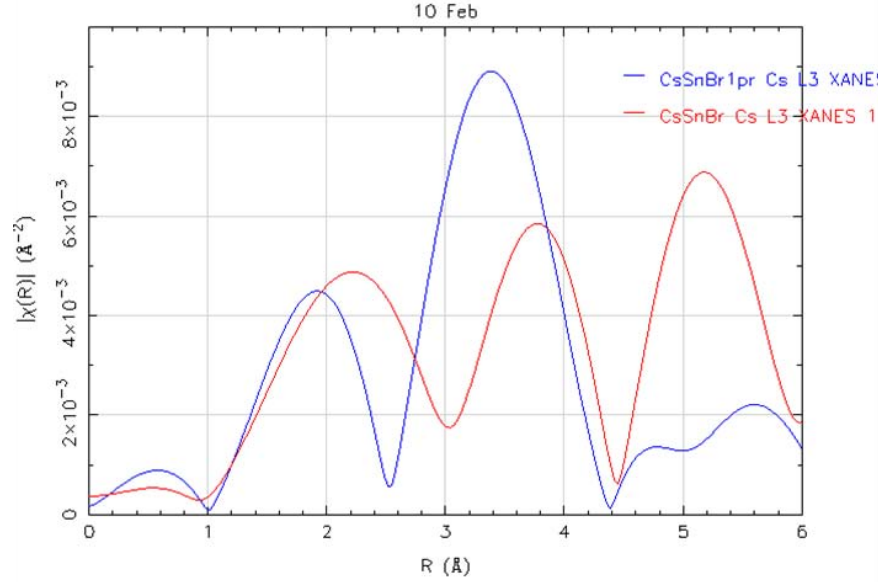
Figure 27. The fits for both CsBr:Sn-1% in blue and $CsSnBr_3$ in red show a missing third shell in the CsBr:Sn-1% data.

The data shown here for both Cs and Sn for CsBr:Sn-1% indicates the lack of Sn in the third shell for Cs and Br at the same location for both Cs and Sn. This suggests a couple of scenarios for where the Sn could be in the crystal. First, it could be shown that the Cs is missing in the Sn centered data which should be about 5.0-Å. The data does not produce any shells past the first shell due to the data truncation for the Ca impurity for CsBr:Sn-1%. This means the Cs could be where it's expected to be. However, the Cs centered data suggests another scenario. Since the Sn is missing and the Br shell is relatively close to where it is supposed to be in both Sn and Cs data for $CsSnBr_3$ the Sn could be taking the place of Cs in the crystal structure as a dopant.

The second scenario is likely due to the probability of the crystal structure shift from CsBr to $CsSnBr_3$ as higher concentrations of Sn is added as a dopant. In this experiment only 1% molar weight Sn is in the CsBr matrix. As the dopant percentage increases the Sn molar weight equals Cs when it reaches $CsSnBr_3$.

The distance of the Sn to Br in the CsBr:Sn-1% was found by averaging the four distances found in the data presented in Figure 26. The distance values fell very close to each other. Thus, a new theoretical value for distance needs to be established for this type of crystal. The distance between Sn and Br is 3.1±0.2-Å. The value presented here is in between the distance of 4.1-Å Cs and Br of the $CsSnBr_3$ and a distance of 3.7-Å between Cs and Br in CsBr with no Sn.

As the Sn^{4+} is inserted into the crystal a phase change occurs as the Sn dopant concentration is increased. The closer distance of the Sn to Br atoms suggests the greater attraction due to the oxidation state of 4+ as opposed to 2+. This does not balance the oxidation of the CsBr or $CsSnBr_3$ unit crystal. That is, Cs^{1+} + Sn^{4+} + $3Br^{1-}$ leaves the charge balance at 2+. The Sn^{4+} does not have to fit into the unit crystal and balance the oxidation state. The positional data points to a modified crystal structure of CsBr existing in a somewhat modified state with a tetrahedral $SnBr_4$ appearing in the matrix in 1% of the concentration. This was suggested in email conversations with Dr. Peter Dowben.

As described earlier, the XANES structure shows the oxidation state of an atom in X-Ray absorption data. By taking truth samples of Sn, SnO^{2+} and tin dioxide $SnO_2{}^{4+}$ and comparing them to the CsSnBr$_3$ and CsBr:Sn-1% samples the oxidation state of the tin is found to be 4+. The EXAFS data for each of these species is plotted below in Figure 28.
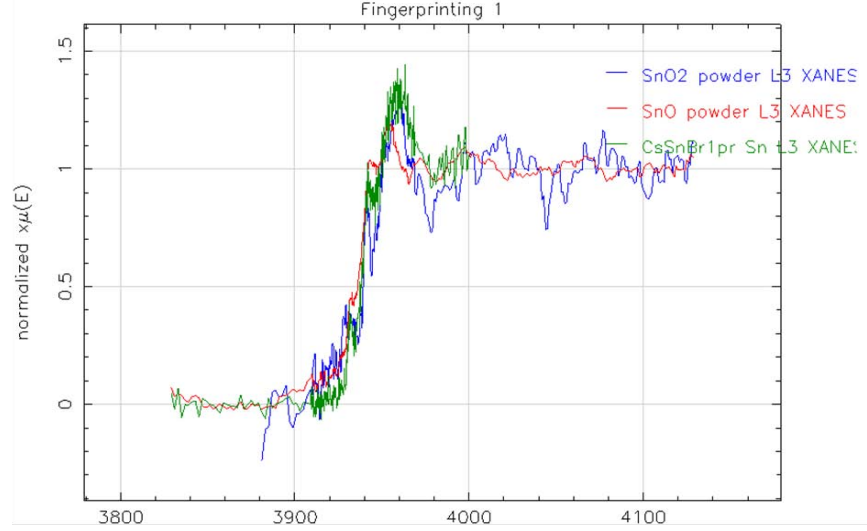
Figure 28. The CsBr:Sn-1% EXAFS data is plotted with SnO^{2+} and $SnO_2{}^{4+}$ powder data. As discussed previously, EXAFS interactions are element specific. Thus the chemical interactions of the oxygen, cesium and bromine atoms, respectively, do not contribute to the shift in the XANES structure. The shift is due to the lack of two electrons as compared with Sn^{2+}. The CsBr:Sn-1% with the Sn^{2+} configuration has been studied in previous literature [Savchyn et al., 2007]. Thus it is easy to deduce the oxidation of the Sn^{4+} oxidation in the CsBr:Sn-1% samples.

The CsBr:Sn-1% EXAFS data is plotted with SnO^{2+} and $SnO_2{}^{4+}$ powder data. As discussed previously, EXAFS interactions are element specific. Thus the chemical interactions of the oxygen, cesium and bromine atoms, respectively, do not contribute to the shift in the XANES structure. The shift is due to the lack of two electrons as compared with Sn^{2+}. The CsBr:Sn-1% with the Sn^{2+} configuration has been studied in previous literature [Savchyn et al., 2007]. Thus it is easy to deduce the oxidation of the Sn^{4+} oxidation in the CsBr:Sn-1% samples. The following figures break this concept down to see the shift in the XANES structure. First, a comparison of SnO^{2+} to the CsBr:Sn-1% is plotted.
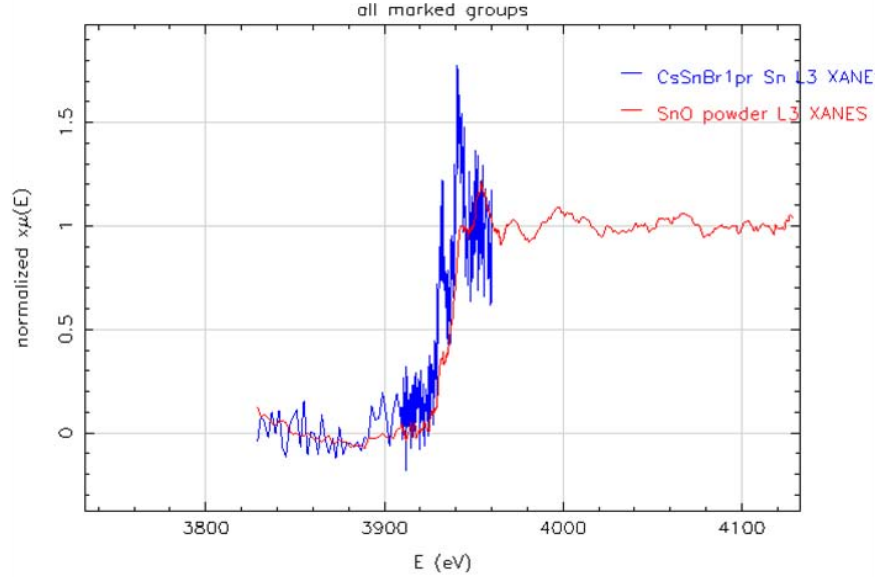
Figure 29. The CsBr:Sn-1% EXAFS data is plotted with SnO^{2+} powder data. The SnO^{2+} XANES structure shows up to the right of the Sn^{4+} of the CsBr:Sn-1%.

Figure 29 is a clearer example much like the Chromium example shown in Figure 5. The different valence state of the tin changes the band structure of the crystal. Thus the scintillation product is different as shown in the Cathodoluminescence results section. Further studies need to be carried out to map the band structure of this material in the Sn^{+4} configuration.

Figure 30 shows the comparison of CsBr:Sn-1% to $SnO_2{}^{4+}$. The XANES structures in this examples line up at the exact same energy. Since, the X-Ray interaction with the L-III edge of Sn, and more specifically Sn^{+4}, the XANES comparison of Sn in different materials can be made.
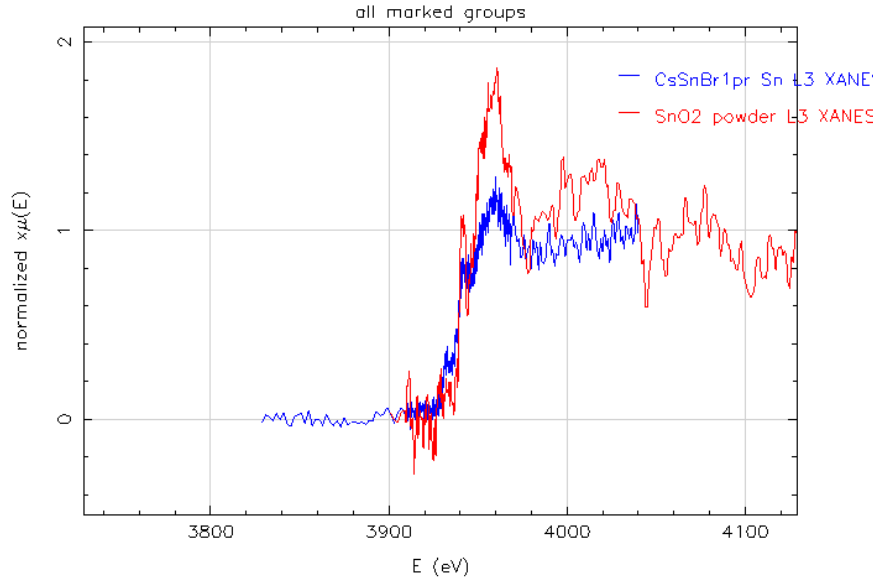
Figure 30. The CsBr:Sn-1% EXAFS data is plotted with $SnO_2{}^{4+}$ powder data. The $SnO_2{}^{4+}$ XANES structure overlays the Sn^{4+} of the CsBr:Sn-1%.

The XANES fingerprinting analysis is straight forward as long as well characterized truth samples are available. Along with SnO_2 and SnO powder samples, an Sn powder sample was also used. The Sn was used as a practice set of data to learn EXAFS processing. There were plenty of samples of known oxidation used in this study.

4.2 Cathodoluminescence Results

The CL for CsBr:Sn-1% provided some interesting results. The oxidation state of Sn in 4+ was expected to change the expected results for the CL curves as compared to the Savchyn et al. [2007] data which has Sn in the 2+ oxidation state. The peaks were expected to shift to slightly higher energies due to the higher Coulomb force on the pulling on the inner electrons. This was observable in the main peak when the experimental data is compared to Savchyn et al. [2007] data. Figure 31 is the Savchyn et al. [2007] data a 290K.
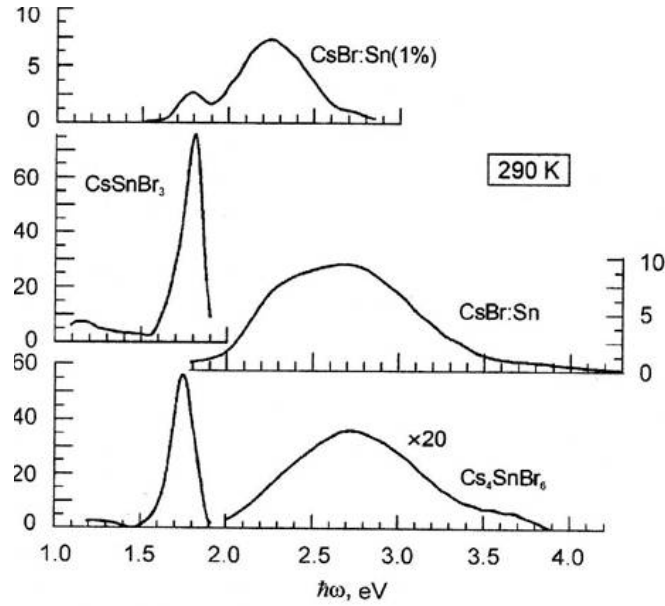
Figure 31. Here is the published data from Savchyn et al. [2007] for comparison with the thesis data. The graph of interest is the top graph.

The most notable peak occurs around 2.2 to 2.3-eV. Another minor peak occurs at 1.8-eV. These peaks occur at the green and red portion of the electromagnetic spectrum respectively. These crystals could be used for scintillation research as photomultiplier tubes sensitive in this region. Most PMTs are sensitive in the blue region of the electromagnetic spectrum. The green peak would work well with a Si based focal plane array detector like a Hamamatsu MPPC module (See Appendix E for a description of the Hamamatsu MPPC module). The CsBr:Sn 1% crystal used in this thesis show some promise in this respect. Figure 32 displays the results of the CL data analysis.
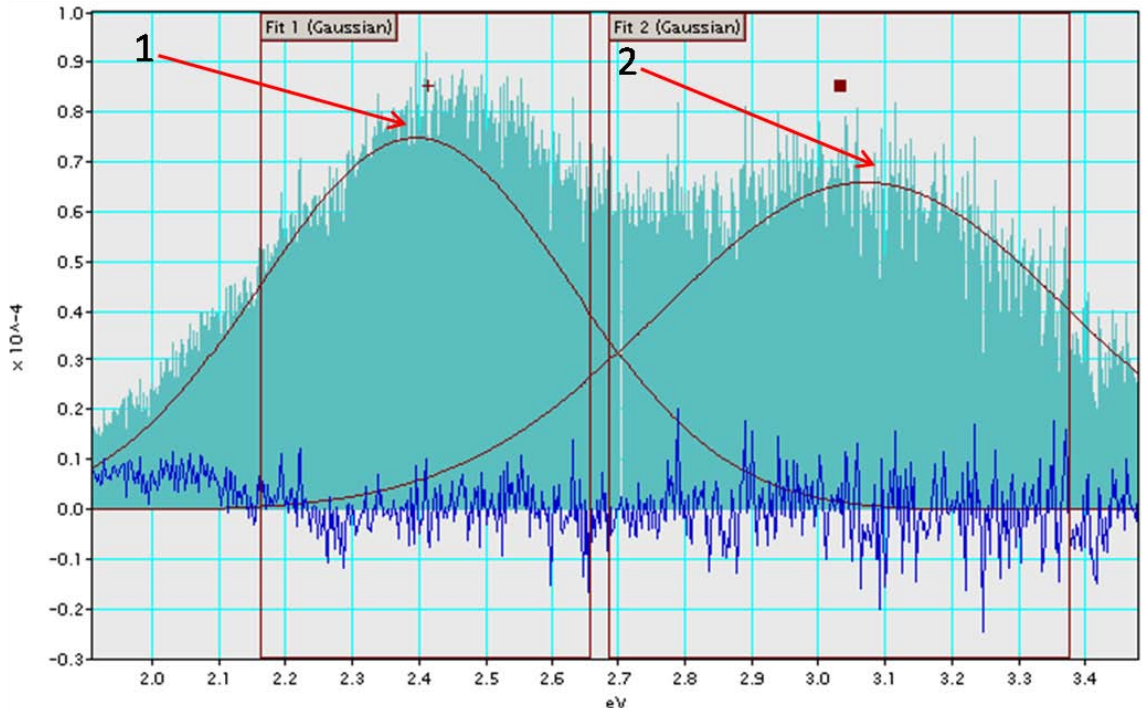
Figure 32. The data for CsBr:Sn-1% shows a peak at 2.4-eV which is at arrow 1. A second peak occurs at 3.1-eV at arrow 2. This Figure was produced using the Gatan monoCL SP Software. These peaks occur close to the Savchyn et al. [2007] peaks in Figure 31. The y-axis is in arbitrary units.

There is overlap between the responses of the Savchyn et al. [2007] data and the experimental data around 2.3-eV. The dominant peak occurs around 2.4-eV as figure 32 shows for the thesis data. A subtle shift towards the blue end of the visible part of the electromagnetic spectrum is noticed. Yet, this change was expected to be a little more drastic due to the oxidation state of the Sn in 4+. Another peak is found at about 3.1-eV which is in the violet part of the visible spectrum. Although less intense than the green peak, the violet peak may be used for further scintillation research. It is not known if either peak is a short decay or the product of a long decay.

It is questionable if the 1.8-eV peak in the Savchyn et al. [2007] data was reproduced in the data taken during experimentation. The monoCL instrument is sensitive in the region including 1.8-eV. The electron excitation state for the 1.8-eV may not exist in the CsBr:Sn-1% with Sn^{4+} sample. Further studies in electronic structure for the occupied orbital states for when the crystal is excited are needed. Figure 33 shows the data below 2.0-eV for CsBr:Sn-1%.
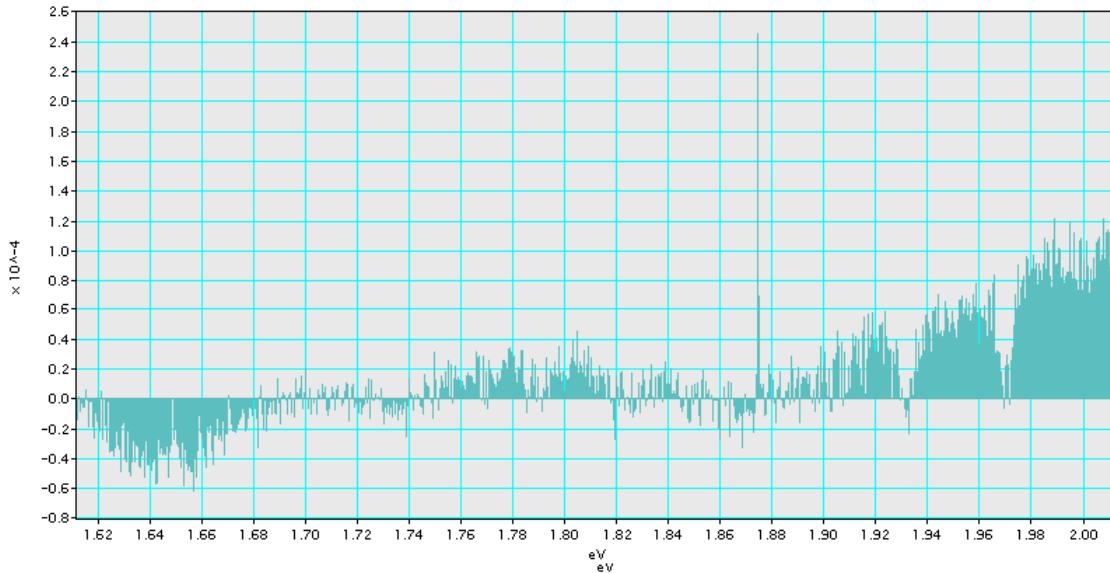
Figure 33. The 1.8-eV peak may be showing in this figure. Figure 34 shows a MATLAB mesh of the data. The negative values suggest a poor response of the monoCL instrument in this range. The calibration only covers the visible range out to red. Any value beyond this is questionable as the linear response of the CCD cannot be guaranteed.

The negative values of intensity in Figure 33 can be explained by poor detector response in the regions they occur in. The 1.8-eV peak would be found in this area. There are some positive counts in this area. A MATLAB code was used to mesh the two data frames together to see if the 1.8-eV peak existed. A couple of points should be noticed first. The data in Figure 33 spans 1.6 to 2.02-eV as compared to 1.9 to 3.4-eV of Figure 32. When the two data sets are merged the intensity of a possible 1.8-eV peak becomes apparent. Figure 34 shows the merged data sets.
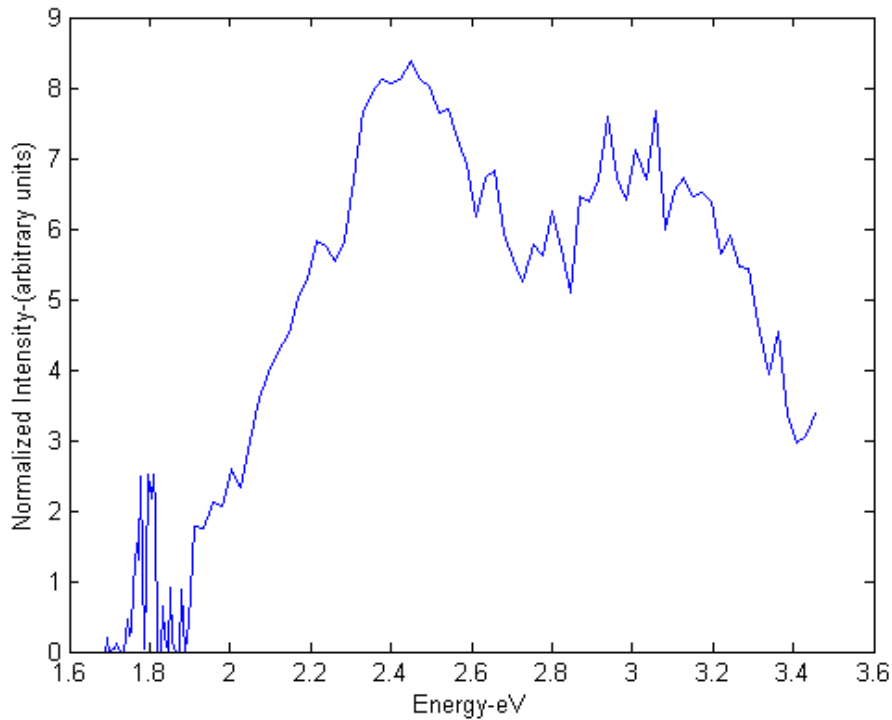
Figure 34. When the two separate CL data sets for CsBr:Sn-1% are merged and scaled the 1.8-eV peak found in the Savchyn et al. [2007] data starts to show. The scaling factor was 10^4.

If there is a 1.8-eV peak it is a very weak response. The Savchyn et al. [2007] data also shows a low response for the 1.8-eV peak. A Gaussian fit could not be performed in Figure 33. The response in the 1.8-eV region in Figure 34 doesn't appear to be Gaussian and rather looks like a noisy response. Thus it is debatable if it exists in the

thesis data. A calibration source for this area of the spectrum may help obtain better data. The calibration source available with the SEM goes to 680-nm, or 1.8-eV. So the calibration ends right at the region of interest.

V. Conclusions

5.1 Experimental Review

The first objectives of this thesis were to find the structure of the CsBr:Sn-1% crystal and associated Sn oxidation state. This was done through EXAFS and XANES analysis. A comparison to the known structure of $CsSnBr_3$ and CsBr was used to determine the position of the Sn in the CsBr:Sn-1% crystal. It was found to be distributed fairly regularly throughout the crystal structure. The XANES analysis lead into the possibility of spectrum changes in CL data. This was observed in the experimental data.

The second objective was to take CL data on CsBr:Sn-1% and $CsSnBr_3$ to compare the results to the published data from Savchyn et al. [2007]. It was expected to see a shift to higher energies for the predominant peaks for both crystals as the Sn was in the 4+ oxidation state. The advantage of higher energies in the spectrum suggests the use of these crystals with traditional PMT systems or Si detector systems for nuclear detection.

Secondary objectives of impurity studies and photoluminescence were also performed. The XRF technique was used to search the crystals for a Ca impurity which was indicated in the EXAFS data for CsBr:Sn-1%. Calcium was found in both crystals at very low concentrations. The effect of these impurities was not explored. Due to the very small amounts, there probably was no effect. Further research should confirm this.

Photoluminescence using gamma ray producing isotopes was also performed. These experiments should be performed again with a couple of changes. First, attenuators should be used between the source and the crystal. This should increase the chance of gamma ray interaction. Larger crystals should also be used to increase the interaction

probability. The use of a UV excitation source could also be benificial. The energy required to excite electrons to cause the spectra noticed in CL measurements lies in the UV range. Reproducing the CL data with photon source, such as UV or gamma ray sources, would be interesting for comparison with CL spectra.

5.2   EXAFS and XANES

The EXAFS data suggests the structure of the CsBr:Sn-1% places the Sn atoms 3.1±0.2-Å from the Br atoms while taking the place of a Cs atom in the matrix. This only occurs 1% of the time as the dopant is 1% of the molar weight. The only limitation of the EXAFS data is the lack of data beyond k values of 7-Å^{-1}. EXAFS is easier and more accurate with k values out to 12-Å^{-1} or more [Kelly, 2009a]. This is a limitation in the case of the CsBr:Sn-1%, Sn centered data. A Ca impurity tainted the data at 4040-eV. The data was truncated per procedure leaving k data values to around 7-Å^{-1}. The other crystals in the study, including the Sn known comparison samples, were also lacking in higher k values. Higher k values make the fitting of theoretical calculations more accurate. The first shell fits are not difficult with the data provided for this study. Measurement past the second shell was not obtainable.

Knowing the electronic structure has lead to some insight on the shift of the CsBr:Sn-1% CL data with the Sn^{4+} configuration. With two less electrons in the outer shells of the Sn, the inner shell electrons would be more tightly bound due to Coulomb force attraction. A higher energy is needed to excite the new electron shell positions. Thus, the spectrum is blue shifted. The CsBr:Sn-1% with Sn^{4+} is superior to Sn^{2+} due to the ease of detecting blue light via PMT than red or infrared light found in these crystals at Sn^{2+}.

5.3 Cathodoluminescence

The CL data provided some interesting results as compared to the Savchyn et al. [2007] data. The subtle blue shift of the predomiinant green peak from 2.25-eV to 2.4-eV and a new peak at 3.1-eV make the crystal attractive for scintillation use. The blue shift is probably due to the closer electron orbits caused by the Sn^{4+} in the crystal as found through XANES. Mating the crystals to visible PMTs sensitive in the blue region or Si based detectors sensitive in the green region, like a Hamamatsu MPPC detector would be benificial. Some Hamamatsu MPPC data was take and is presented in Appendix G.

Future studies could include a look into the CsBr material response at cryogenic temperatures to compare with the Savchyn et al. [2007] data . Room temperature was used in this study as the material would be intended to be used at this environment. Cryogenic cooling was not performed due to the SEM/CL instrumentation. The SEM/CL instrumentation only supports room temperature measurement. However, a CL instrument is being assembled by the Physics department and will be completed in the near future.

5.4 Recommendations for Future Research

In summary, the use of CsBr:Sn-1% as a scintillator material looks promising. The crystal has a low light yield, as found in CL experiments, but the relaxation times of the electrons need to be studied. Measuring the decay time could prove an advantage of using CsBr:Sn-1% as a scinitillator. Other experiments should be performed to measure linearity, resolution, efficiency and light yield. Larger crystals with favorable geometries would make these measurements possible. A larger crystal size provides an increased probability of gamma ray interaction. A large cylindrical shaped crystal could be optically coupled to a PMT for better analysis.

Appendix A. EXAFS and XANES

This section will derive, in short, the physics and math behind EXAFS analysis. The basic physics behind x-ray and subsequent photoelectron interaction were described earlier. The derivation of the math is based on quantum physics treatments with fairly straight forward outcomes. A good treatment can be found in Als-Nielsen and McMorrow [2001].

$$\chi(k) = \sum_j \frac{N_j e^{-2k^2\sigma_j^2} e^{R_j/\lambda(k)} f_j(k)}{kR^2} \sin[2kR + \delta_j(k)] \tag{A.1}$$

A quantum mechanical treatment can be used to derive the EXAFS equation. This derivation is taken from Newville [2004] and Als-Nielsen and McMorrow [2001]. The Newville [2004] work has a quicker and easier to understand version.

First, it is assumed the initial photoelectron wave has an initial state $\imath$. When acted on by the operator $\mathcal{H}$ and a final state. This is proportional to $\mu(E)$ described Fermi's Golden rule.

$$\mu(E) \propto |\langle i| \mathcal{H} |f\rangle|^2 \tag{A.2}$$

Taking the neighboring atoms into account on the final state of the atom, f can be broken into f_o for the interaction with the isolated target atom case and Δf for the expected interaction with the neighbor represented here:

$$|f\rangle = |f_o + \Delta f\rangle \tag{A.3}$$

When Equation A.3 is expanded a few terms become apparent.

$$\mu(E) \propto |\langle i| \mathcal{H} |f_o\rangle|^2 \left[1 + \langle i| \mathcal{H} |\Delta f\rangle \frac{\langle f_o| \mathcal{H}|i\rangle^*}{|\langle i| \mathcal{H} |f_o\rangle|^2} + Comp.Cong. \right] \tag{A.4}$$

A few relationships fall out of this equation. The first term is the initial absorption. That is, it is the ideal case of the isolated target atom. Thus $\mu_o = |\langle i| H |f_o\rangle|^2$. Using some bra-ket math it can be shown that:

$$\mu(E) = \mu_o(E)[1 + \chi(E)] \tag{A.5}$$

The $\mathcal{H}$ operator is just a change of momentum Energy states which is expected in an excitation, scatter or reflection. Newville [2004] describes the $\mathcal{H}$ operator reducing to e^{ikr}. Since the wave form is a wave term dependent on energy the term $\chi(E)$ which is the fine structure representation. It can be shown as Equation A.6.

$$\chi(E) = \langle i|\mathcal{H}|\Delta f\rangle \tag{A.6}$$

Equation A.6 makes sense as it shows the operator changing the initial state into the scattered states resulting in the fine structure. Switching the bra-ket notation into integral form Equation A.6 turns into:

$$\chi(E) \propto \int dr \delta(r) e^{ikr} \psi_{scatt.}(r) = \psi_{scatt.}(0) \tag{A.7}$$

where $\psi_{scatt.}(r)$ is the wave function of the scattered electron.

The outgoing photoelectron from the originating atom can be represented as a spherical wave function. This is done to evaluate the EXAFS at the neighboring atoms causing the wave-like variation in the post absorption edge structure. ψ of the outgoing photoelectron is shown as:

$$\psi(k, r) = \frac{e^{ikr}}{kr} \tag{A.8}$$

Capital R is used to represent the distances to the neighboring shells. Let's consider the first shell for simplicity so r=R. Since the χ term is the wave after

the scatter we take ψ r=0, but at k or more succinctly put $\chi(k) = \psi(k, r = 0)$. In order to get the scattering in the equation and atomic interactions with the incoming photoelectron the scattered χ term is evaluated as a direct reflection back to the originating atom as this situation is a probability. It also makes the math nicer. Taking all these terms together produces Equation A.9.

$$\chi(k) = \frac{e^{ikR}}{kR} \left[2kf(k)e^{i\delta(k)} \right] \frac{e^{ikR}}{kR} \tag{A.9}$$

Where $f(k)$ and $\delta(k)$ are scattering properties of the scattering atom. The complex conjugate is also added the right of the equation which simplifies to:

$$\chi(k) = \frac{f(k)}{kR^2} \sin[2kR + \delta(k)] \tag{A.10}$$

Yet, there is one more atom in the lattice. The N term is introduced to account for the number of atoms per shell distance R away from the scattering atom. The Debye-Weller, $e^{-2k^2\sigma^2}$, term is also introduced to account for thermal vibrations in the lattice and also covers minute disorder. Subscripts are added to N, R, σ, $f(k)$ and δ. This is done to account for each individual atom's contribution to the final $\chi(k)$. Inelastic scattering must also be accounted for. A mean free path term is introduced to describe the distance a photoelectron travels before scattering. Newville [2004] describes the process in more detail. In short, a factor of $e^{R_j/\lambda(k)}$ is multiplied into the equation to account for these interactions. Each atomic contribution is then summed and the EXAFS equation is derived as:

$$\chi(k) = \sum_j \frac{N_j e^{-2k^2\sigma_j^2} e^{R_j/\lambda(k)} f_j(k)}{kR^2} \sin[2kR + \delta_j(k)] \tag{A.1}$$

A switch to k space is made for the Fourier transform which produces the R data and graphs for visual analysis during fitting. It also solves for the terms described earlier in Table 1. A reverse Fourier transform can be applied to get a cleaner k space sometimes referred to as q space.

Appendix B. EXAFS Data Processing

The suite of programs producing the EXAFS data used in this research include Hephaestus, Athena, Artemis and Atoms [Ravel and Newville, 2005]. Athena and Artemis are the primary programs for data manipulation and theoretical calculation. They are based on the legacy code of IFFETT which is still the basis for most EXAFS processing codes (IFFETT source). A top level overview will be given for processing familiarity.

Calibration of the raw intensity data is the first step in EXAFS process. In the data sets used for the $CsSnBr_3$ and CsBr:Sn-1% were usually within $\pm$1-eV of the expected absorption edge of Cs or Sn data. The data must be smoothed before it is calibrated. The Athena program has an automated function for smoothing, calibration and background subtraction. The first two options are found in the *Data* menu. The unprocessed and smoothed data is shown below in Figure 35.
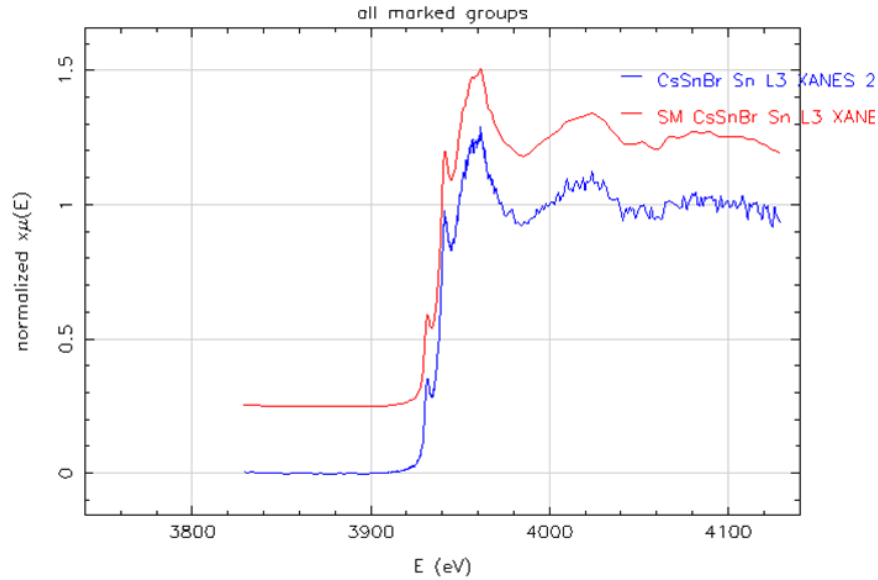
Figure 35. The $CsSnBr_3$, Sn centered raw data is the blue line while the smoothed data is drawn in red. Smoothing is done for calibration purposes. The smoothed data can be used for data processing. An offset value in the y-direction has been used for ease of viewing. Both data sets are normalized.

56

Smoothing is done to get a cleaner spectrum for calibration of the data. The calibration depends on the absorption edge occurring at a maximum derivative of the data around the theoretical edge. A second derivative is taken to find the zero crossing point. If the raw data is noisy it is difficult to ascertain the absorption edge maximum in the first derivative. The next series of images will illustrate the process.
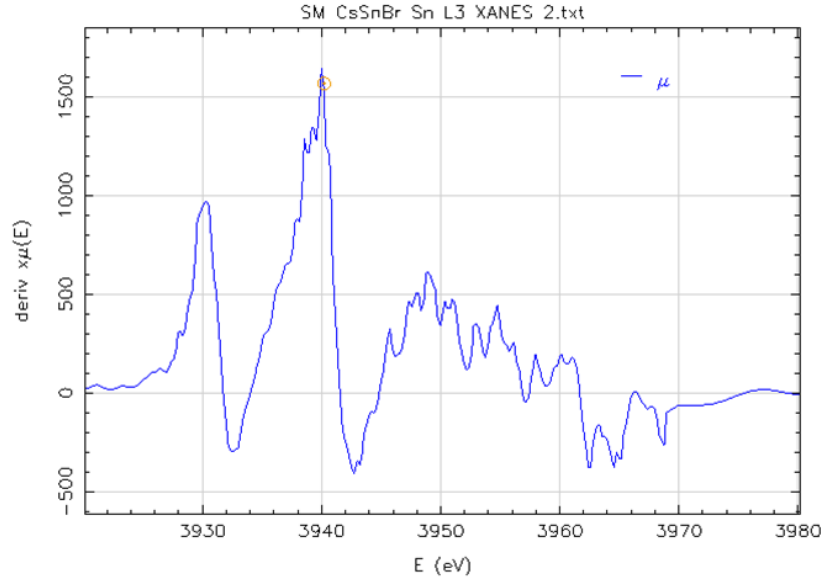
Figure 36. Athena selects a peak around 3840-eV which is far from the 3929-eV value for Sn. Variations in E_o on the order of 10-eV can occur but it is unlikely the case here. There is a maximum closer to 3929-eV which is probably the most likely candidate value for the 3929-eV edge.

From here the second derivative is taken to find the zero crossing point. The zero crossing point is the place where to edge of the absorption for Sn occurs. The calibration of Sn data gives a common reference for EXAFS analysis. The Second derivative is shown in Figure 37.
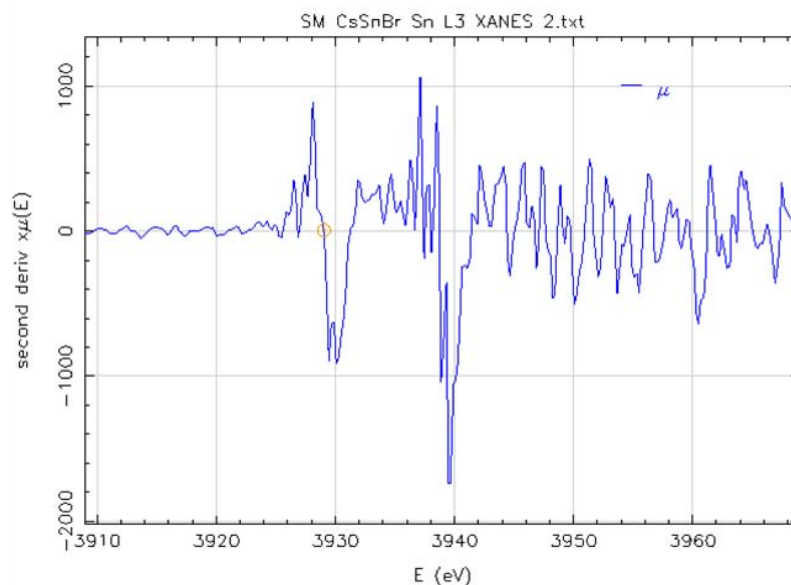
Figure 37. The zero crossing point is the maximum of the first derivative from Figure 36. The second derivative provides a closer value to finding the absorption edge. In this image the zero crossing point has been found automatically with *Find Zero Crossing Point* option with the *Second Derivative* feature selected in Athena. The

Once the zero point is found from the second derivative the data is calibrated to the desired energy absorption edge. The data can now be processed further in Athena. The next few steps of processing define the values to be included in EXAFS analysis. Picking too much data leads to noisy R data and shifting of peaks. Both of these factors can lead to large variances in error.

The next step of EXAFS data processing involves a background subtract of the data and picking a window of k values for the Fourier transform. The background subtract is defined by a handful of factors which are inter-related. Picking the values of these factors is mostly physics based but can also take an artful approach as no two EXAFS data runs are exactly the same. Finding the appropriate k window is totally dependent on the smoothness of the data. Both processes have a profound impact on the data fitting in Artemis.

The background subtraction of the data is first based on the splines of the pre and post edge data in E space. This brings back Equation 2.2. The pre-edge spline, taken from the data before the absorption edge, and the post edge spline, taken from the data after the absorption edge define the $\Delta\mu(E_o)$ term. The pre and post edges must be a straight line or very close to the form of $y = m{*}x + b$. Figure 38 shows the pre and post edge splines.
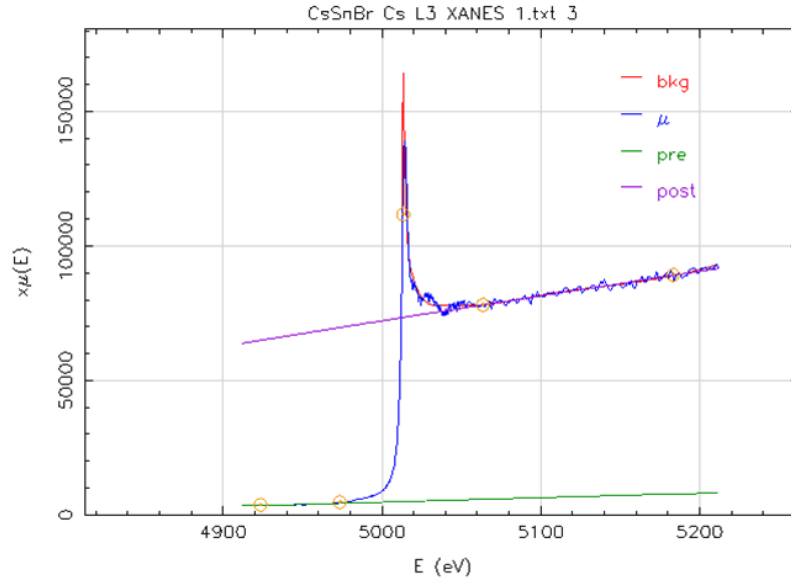
Figure 38. The pre and post edge splines are used to define the edge step term in Equation 2.2, $\Delta\mu(E_o)$ The lines must be close to the form $y = m{*}x + b$. The pre edge spline is the green line. The purple line is the post edge spline and the red line is the background result of Equation 2.2.

The background subtract is done to smooth the data. Picking the pre and post edge splines is important in ensuring certain information is not filtered out. Equation 2.2 is equivalent to the EXAFS equation, Equation 2.4. So the background fit is a theoretical, ideal fit to the data. When it is subtracted, it leaves the very fine structure for analysis. The pre and post edge splines used in defining $\Delta\mu(E_o)$ also represents the normalization of the data. Normalization is the process of reducing the effects of several x-rays down to one x-ray. This also reduces the photoelectron scattering process down to one photoelectron resulting from the one x-ray on the target atom.

The next process is picking the k window. The k window is a filter of data for EXAFS processing past the absorption edge. The EXAFS structure begins around 100-eV past the absorption edge. The XANES structure does contain some first shell reflection but its amplitude is too large to account for EXAFS interactions. These first shell reflections and scatters are also contained in the EXAFS region so they are not lost by filtering out the high amplitude information. Thus the lowest k value is chosen where the fine structure data does not vary widely. This is done by varying E_o by small amounts with a small k-weight factor, usually 1. The lower k values are closer to the XANES structure. Thus, there is great variability in the amplitude of the data. By finding the point at which the k data is consistent, or close, the high amplitude data can be filtered out. Varying the E_o parameter shifts the k drastically in the XANES structure but not in the EXAFS data. Figure 39 shows the graphical process.

The k weight is a multiplier of the $\chi(k)$ function after the Fourier transform. The k weight emphasizes shells depending on the chosen weight. Lower k numbers emphasize closer shells. Conversely, higher k weights emphasize further shells. The correspondence between k weight and shell number is pretty much close to 1:1. That
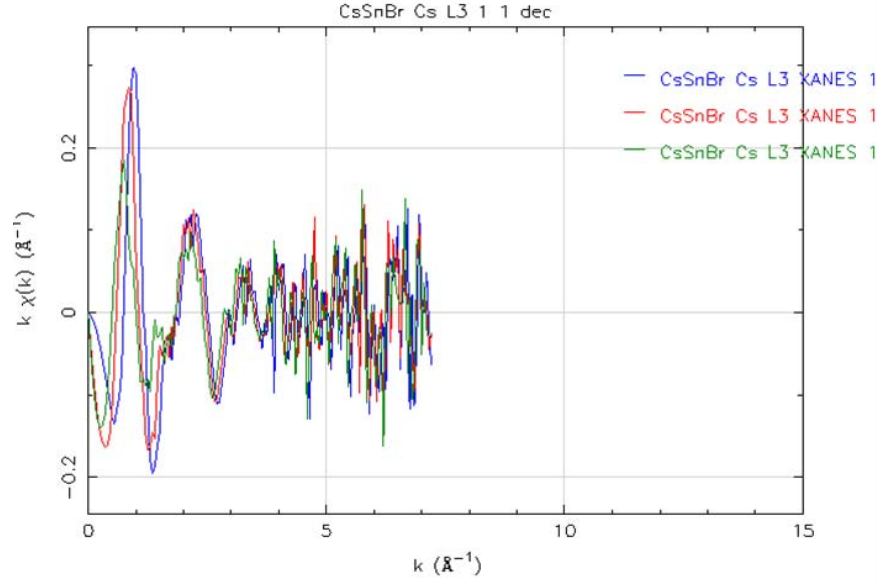
Figure 39. **Picking the low k value for the Fourier transform involves some eyeball work. The data provided for the thesis is noisy. Yet, getting close enough will have to suffice. The low k value which fits the criteria would be about 3.5-$\mathring{A}^{-1}$. This is where the data does not change drastically based on small E_o shifts. The usual low k values are between 2-4-$\mathring{A}^{-1}$ [Kelly, 2009a].**

is, a k weight of 2 corresponds to the second shell. This is true for crystals with largely spaced radial distributions. Radial spacing greater than 1-$\mathring{A}$ were found to follow this correspondence. The k weight is not a direct multiplier but rather an power multiplier. A k weight of 2 means the $\chi(k)$ function will be multiplied by k^2. A k value of zero is also possible.

The selection of low and high k values is not to include too much data to create noise. Conversely, excluding data with a narrow k window will leave out important information on neighboring shell information. Having k data which extends far is a must. Achieving high k values means scanning into higher energies past the absorption edge. The EXAFS region can extend to 1000-eV. Maximum k window values are usually between 10-14-$\mathring{A}^{-1}$ [Kelly, 2009a]. Maximum k window values are chosen by a similar process as the minimum k window values. The difference is using the

highest k weight at which the data will be analyzed. The E_o value does not have to be changed due to its small effect on k data past 5-$\overset{\circ}{\text{A}}^{-1}$ or so. The max overall k values for the data provided for this thesis didn't go past 7-$\overset{\circ}{\text{A}}^{-1}$ very much.

Another important factor is the choice of R-Background defined as the value Rbkg in Athena. The Rbkg number removes the Fourier components below the desired value [Ravel and Newville, 2005]. Usually, the Rbkg is half the distance to the first shell [Kelly, 2009a]. Choosing an Rbkg too far from this value will reduce the amplitude of the R value in the shells [Ravel and Newville, 2005].

After the appropriate values are determined in Athena the data is passed into the program Artemis. Artemis is where the theoretical calculations of crystal structure are made and compared to the real world data. The crystal structure is defined by the space group and atom distribution within the crystal group. The web service ATOMS is used for defining the crystal structure. ATOMS is imbedded with Artemis but is easier to use on the world wide web. The web service also includes a library of crystal structures. The only crystal structures available in the library for this thesis were for the βSn, SnO and SnO_2 powders. An example for Cs centered $CsSnBr_3$ is shown in Figure 40.

The crystal properties, as described earlier, are entered into the top half of the template. The $CsSnBr_3$ atoms file is being created in this example. Cesium is the central atom for this file and is put at the origin. The Br atoms are found on faces of the cube structure. To define the Br positions only one position is needed. The software does the work of placing the other Br atoms in their correct position. The Br atoms are half the crystal lattice constant distance in one dimension and half the distance in another. The xy plane was chosen here. The Sn atom is another half distance in the z direction. The run button is clicked and a text file is generated which can be cut and pasted into the Artemis program or saved for later in a *.txt

Figure 40. Creating a crystal structure in the webATOMS service and copying the output into Artemis is the easiest way to get the theoretical calculations started.

file. Another ATOMS file is needed for the Sn centered data. This is due to the radial distribution differences from a Sn centered perspective. In a Cs centered crystal the closest, first shell Br atoms are $\approx$ 4.1-Å. In a Sn centered perspective the first shell Br atoms are $\approx$ 2.9-Å. The R plots in EXAFS will look drastically different between Cs and Sn centered perspectives.

After the EXAFS data has been processed in Athena it is loaded directly into Artemis for theoretical comparison. The ATOMS file is loaded under the Theory menu, New FeFF template option. Once the calculate button is hit the photoelectron paths are generated. Usually, 10 paths or less are used to fit the first 2 or 3 shells. It is usually best to use paths that are less than or equal to the shells being analyzed. The paths are displayed in Figure 41.

The fit for this run of $CsSnBr_3$, focusing on Cs, is shown in Figure 42. The first shell is actually the third peak from the left. The first two peaks are half scattering paths of the first and second shells. An option of fitting the background
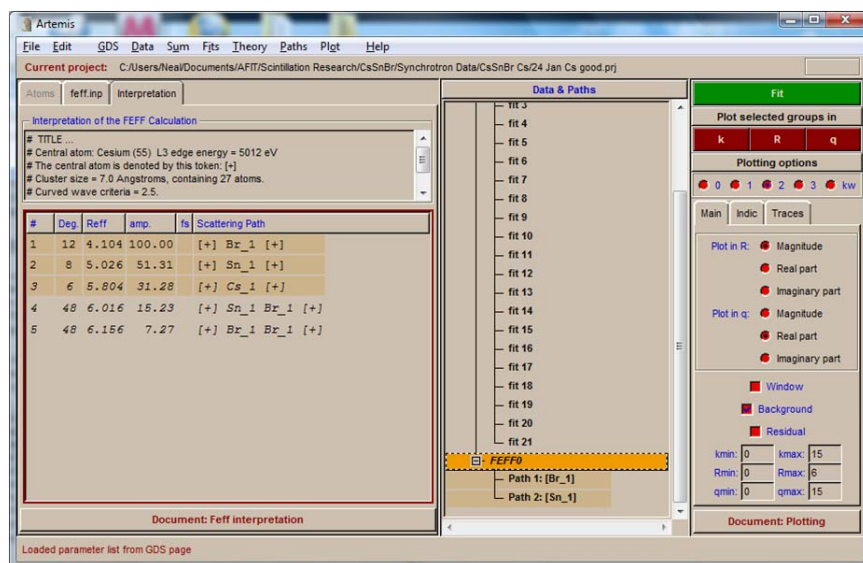
Figure 41. The lower left box shows the paths generated from the ATOMS file obtained from the web. A total of 27 atoms in 3 neighboring shells were used to generate the paths. Path 1 is to the first neighbor atoms of Br. The last two pats are made up of scatter paths. For example, path 4 is the scattering path of the photoelectron scattering off a Sn atom and then a Br atom.

function suppresses the Fourier transform window that was defined in Athena. The suppression will include the background data before the Rbkg value for fitting.
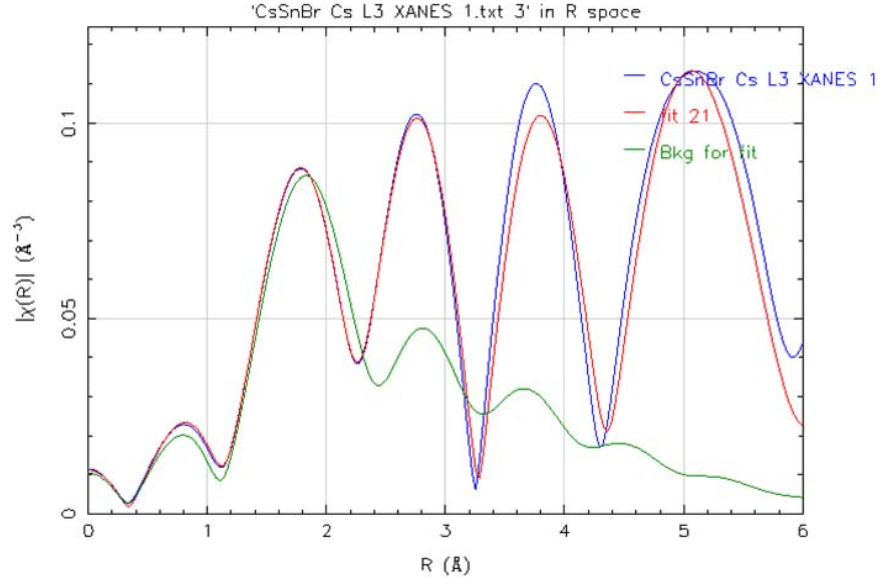
Figure 42. This is a close to good CsSnBr$_3$ fit using the Fit Background option.

Table 7. Close CsSnBr$_3$ fit

R	4.2-Å
ΔR	0.12-Å
σ^2	0.034-Å^2
N	12
ΔE_o	1.04-eV

The final fits are presented in the analysis section for CsSnBr$_3$. The fits are much different do to the resizing of the k window. It was found that after several fits closer values for R and σ^2 could be obtained if the

Appendix C. XANES Analysis of CsSnBr$_3$

The charge of the Sn in CsBr:Sn-1% was a particular focus of the thesis study. The change of Sn oxidation state was thought to have an effect on the luminescent properties of CsBr:Sn-1%. CsSnBr$_3$ was not looked at as a scintillator due to its opaque nature. Thus, the charge state and the related effects were not looked at. This appendix will take a quick look to show the Sn is also in a 4+ oxidation state in the CsSnBr$_3$ crystal. Following the procedures described earlier, the CsSnBr$_3$ was compared to $Sn0^{2+}$ and $Sn0_2^{4+}$. Figure 43 compares the x-ray aborption spectra of all three structures.
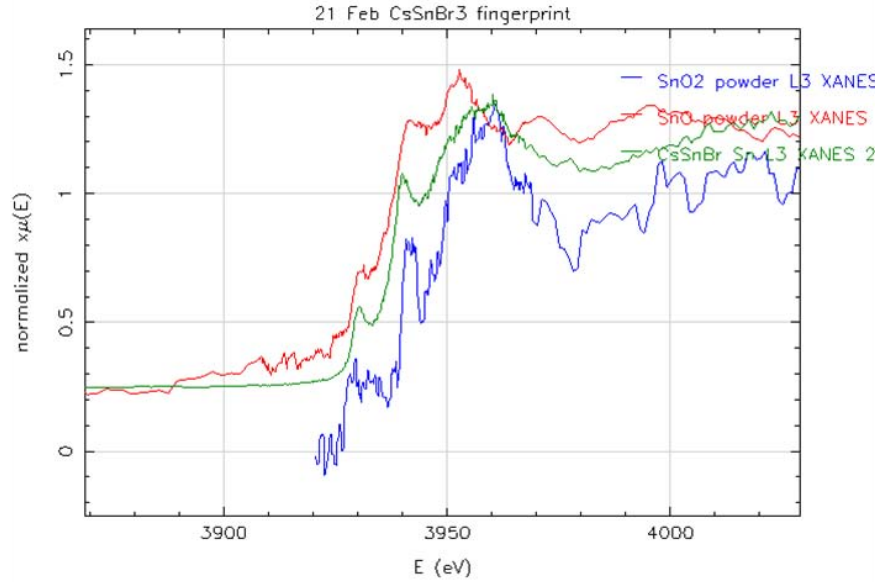
Figure 43. In this figure a comparison of all three compound x-ray absorption spectra are shown. The Sn in the CsSnBr$_3$ is found to be in the 4+ oxidation state. Figures 44 and 45 show a closer look.

Comparing the CsSnBr$_3$ with SnO and SnO$_2$ individually is shown in Figures 44 and 45. The XANES structures of SnO$_2$ and CsSnBr$_3$ line up to indicate the Sn in the 4+ oxidation state.
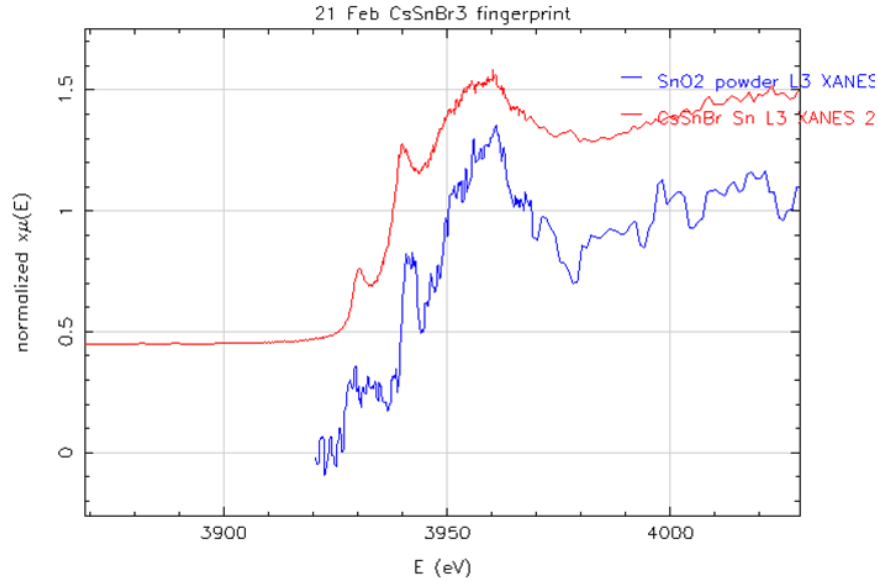
Figure 44. The data for SnO$_2$ was truncated at 4040-eV. The data before this point was causing the normalization of the spectra to be much higher than what it should be. The XANES structures lineup showing the Sn in the CsSnBr$_3$ to be in the 4+ state.

The SnO XANES structure is found to the left the CsSnBr$_3$ XANES structure. As with CsBr:Sn-1% a different structure may be possible to allow Sn^{4+}. However, the EXAFS analysis showed the CsSnBr$_3$ structure to match the Pm3m crystal structure as expected. Figure 45 shows the shift of the CsSnBr$_3$ XANES structure as compared to SnO.

The charge imbalance phenomena may have a couple of explanations. In the case of CsBr:Sn-1% the Sn^{4+} may be bonded in tetrahedral structures throughout the crystal per communications with Dr. Peter Dowben. Instead of Cs in a unit crystal, Sn my take its place to make a SnB4$_4$ structure within the CsBr crystal lattice. In the case of CsSnBr$_3$, a Cs may be missing from the unit crystal structure to allow a Sn^{4+} atom.
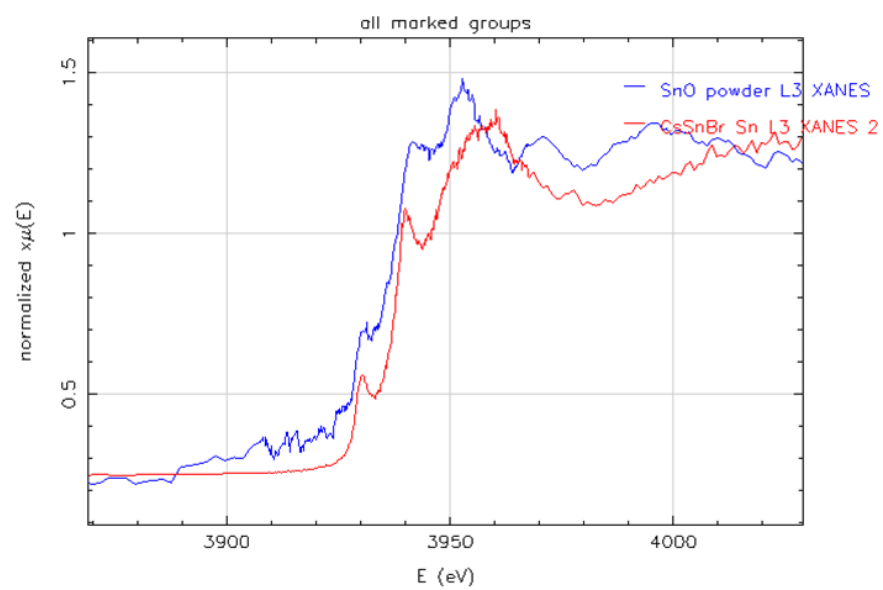
Figure 45. The SnO XANES shows the shift of the Sn in CsSnBr$_3$ to 4+ oxidation state.

Appendix D. Cathodoluminescence Data Processing

A conversion from wavelength to energy requires a multiplicative factor of λ^2. This can be seen by looking at the quantum theory of light with respect to energy as a function of wavelength. Equation D.1 shows the dependence of E:

$$E = \frac{hc}{\lambda}, \tag{D.1}$$

where E is energy, h is Planck's constant, c is the speed of light and λ is the wavelength. The conversion from wavelength to energy must be taken with respect as a change of energy over a change in wavelength between intensity differences. So the derivative of Equation D.1 must be taken as

$$\frac{dE}{d\lambda} = -\frac{hc}{\lambda^2}. \tag{D.2}$$

Since energy can be related to intensity by a constant multiplier a change of intensity per change in wavelength can be substituted into Equation D.1 as:

$$\frac{dI}{d\lambda} = K\frac{1}{\lambda^2}. \tag{D.3}$$

where the K multiplication factor absorbs the negative sign and the constants of hc. The value of dI is the change of intensity. When this is solved for the change of wavelength, which is a function of energy, the relation turns into:

$$d\lambda = K\lambda^2 * dI, \tag{D.4}$$

where K is still an arbitrary constant. Thus, for any change in wavelength as a function of energy the intensity at a particular wavelength must be multiplied by a factor of λ^2.

Appendix E. Photoluminescence Data

The photoluminescence data taken on CsBr:Sn-1% and CsSnBr$_3$ showed noise throughout the visible range. A few improvements are needed in these experiments to make the photoluminescence results conclusive. The use of attenuators could provide a higher probability of gamma ray interaction. A larger crystal would also help in this matter. Once these requirements are met, further experimentation should be performed. The experiments did provide some insight on other crystals with scintillation potential.

Half way through the research newer samples of CsI(CdI$_2$) were provided by Dr. Peter Dowben. These materials are novel with their dopant. CsI is most commonly doped with Tl or Na. Both of these CsI materials are well used and characterized [Knoll, 2000]. The CsI(CdI$_2$) were also thin but were more efficient at scintillating as results in Figure 46 shows.
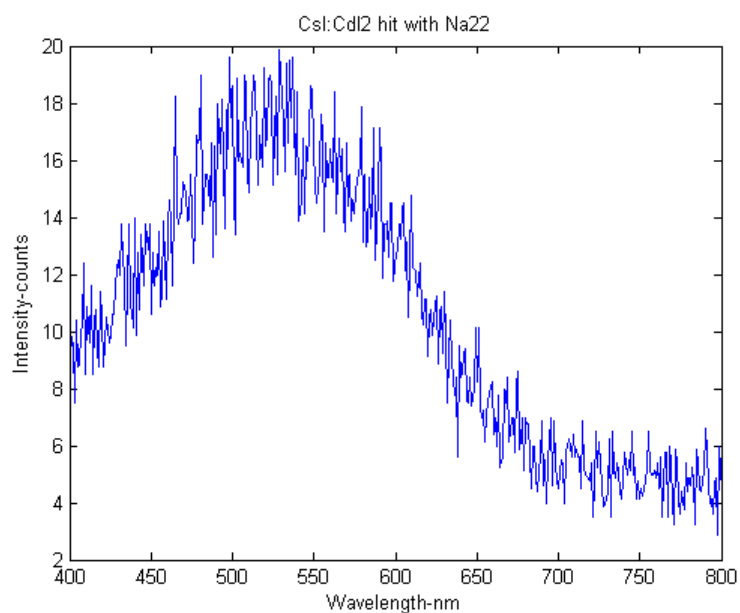
Figure 46. There is a definite difference with the CsI(CdI$_2$) sample. Sodium-22 was used for the excitation. The frame shows the results of 4 averaged runs with 2 second integrations per nanometer step. The peak occurs around 525-nm in the blue.
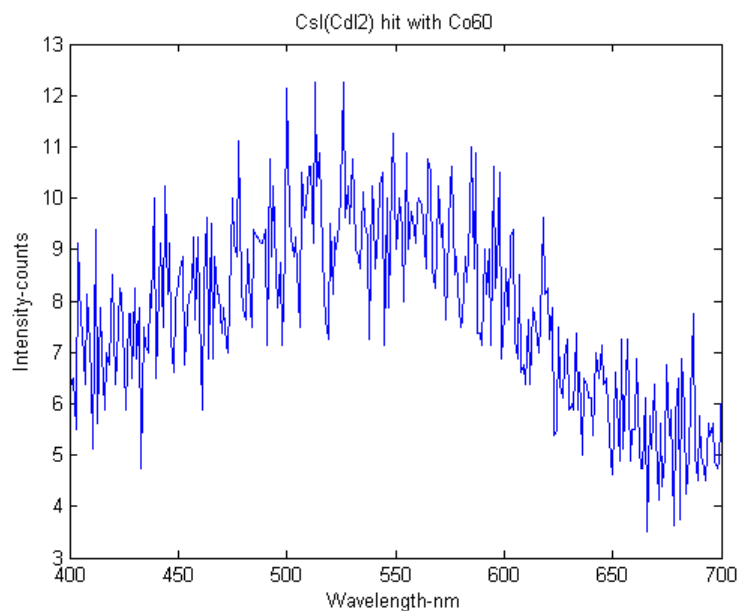
Figure 47. ^{60}**Co was used in this example. A peak is shown to be in the same place with the** ^{22}**Na data. A clearer picture is shown in Figure 48**

71

CsI(CdI2) hit with Co60 (scaled)
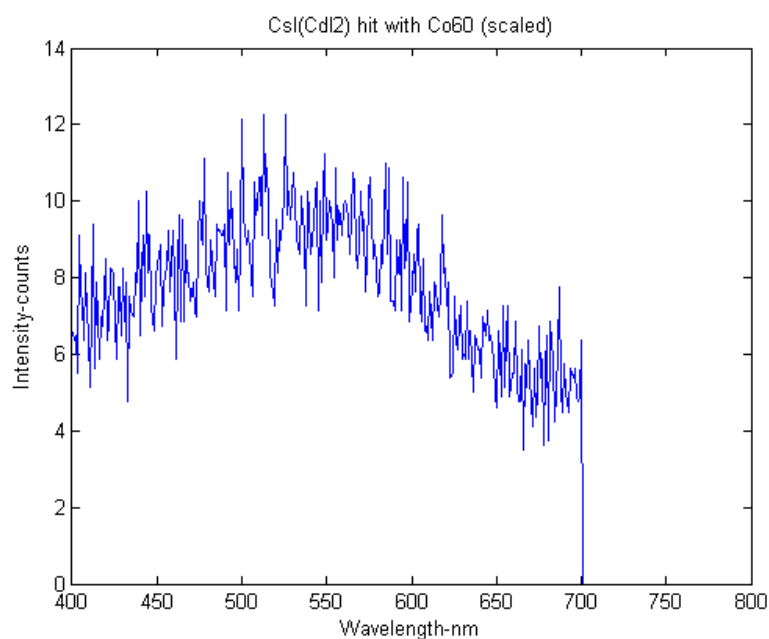
Figure 48. The data is scaled in this figure. The values are set to zero after 701-nm to achieve the same scale as Figure 46. This data set was shorter due to the essence of time. Like the previous two figures the integration time was 2 seconds over 1-nm intervals. The 300-nm bandwidth covered here takes 600 seconds. Four runs are averaged here taking a total of 2400 seconds.

Photoluminescence can be used to measure the visible to infrared, and some UV, luminescent properties of a material when it interacts with a source light or isotope source. In some experimental setups, excitation and relaxation times can be measured. This cannot be done on the AFIT photoluminescence detector located in Building 470. Upgrading and modernizing these capabilities should be considered if excitation and decay times are desired. Figure 49 shows the current system setup.
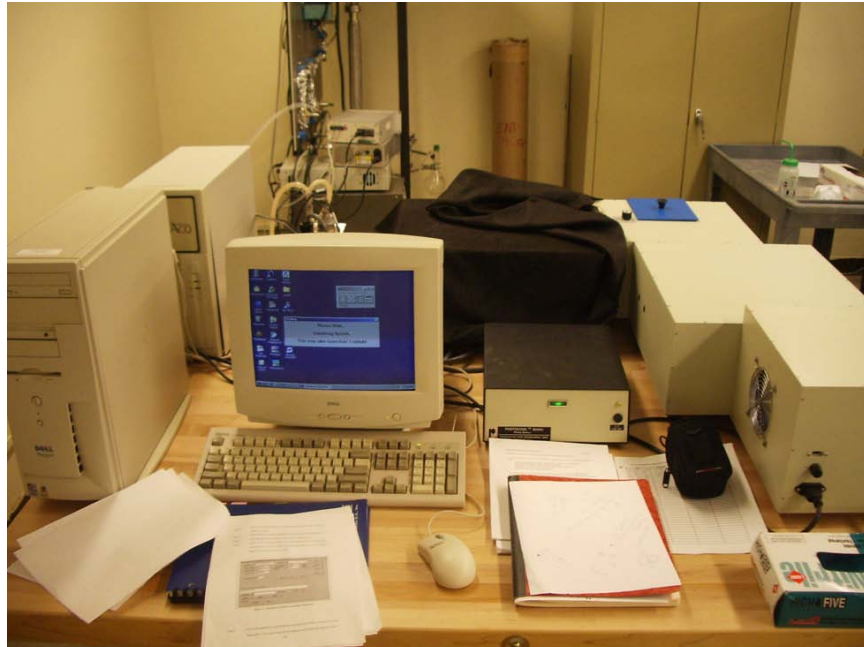
Figure 49. The noise floor once the instrument is cooled is around 5 photons per second per nanometer band gap. In this image the photomultiplier, optics and CCD are located under the black cloth. The sample chamber is under the blue cover. A calibration/source lamp is a couple of modules to the right of the computer. The lamp was only used as a calibration source. Gamma sources such as ^{137}Cs and ^{60}Co were used as excitation sources. These isotopes were mounted with the sample as shown in Figure 50 and then put into the sample chamber facing the PMT box. In order to aid the 5-photon/sec noise floor, the lights would had to be turned out.

Even though there were limitations in the setup of the light table system, meaningful quantitative data can be taken. The light table setup was used as a scintillating detector. That is, it was setup to perform as a scintillating detector. Instead of NaI(Tl) being the scintillating material, the CsBr:Sn-1% was used. The PMT was not optically coupled to the CsBr:Sn-1%. Efficiency due to loss of photons was highly evident as the detectable signal was 20 photons per second. This is a far from what is compared with NaI(Tl) which has 38,000 photons per MEV per interaction [Knoll, 2000].
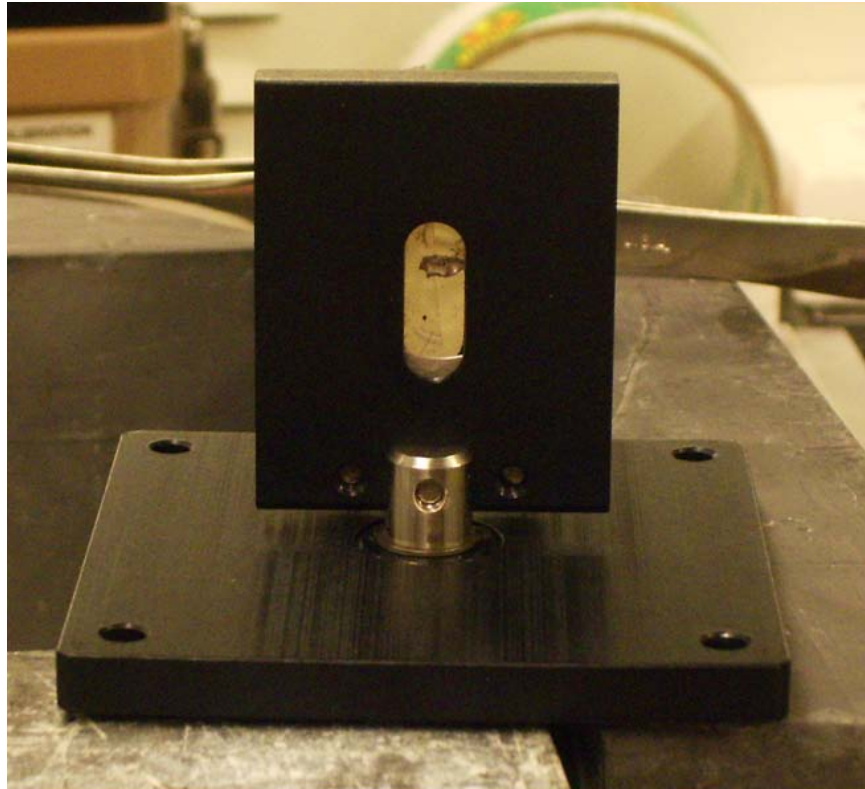
Figure 50. One of three mounting methods is shown here. A custom plastic holder was built to hold planchette sources in order to gain consistency.

The sample mount provided with the light table was not designed to hold the planchette sources and samples all at one time. Teflon tape was used to hold the samples in front of the active region of the planchette source. The planchette source and sample pair were mounted in the sample holder. The teflon tape proved difficult to work with as the samples could slide out of the active region on the planchette source very easily. Inconsistent results were obtained due to the mounting scheme. Thus, the plastic holder in Figure 51 was designed to eliminate most of the hassle of getting the source and sample in the right position.

Figure 51. The customized plastic mount made it easier to change samples and isotope planchette sources. The planchette source holder on the right had a bore down the middle to reduce gamma ray attenuation. If an irregular target sample was used the center block in the frame was used to hold the source in the path of the gammas coming from the bore. Although efficiency was lost due to solid angle losses the consistency of results improved. The mounting scheme worked well for the wafer-like shape of the CsI(CdI$_2$) samples as demonstrated in Figure ??.
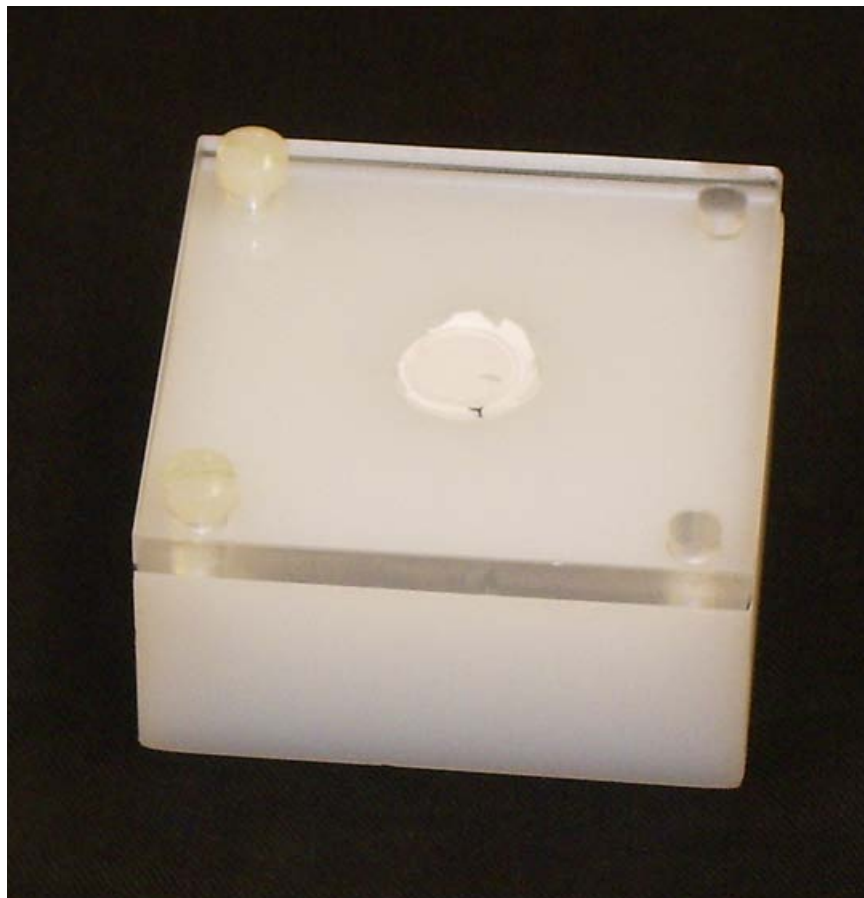
Figure 52. The wafer-like shape of the $CsI(CdI_2)$ samples fit well in the front of the holder. Hobby craft FunFoam was used to stabilize any samples and hold them in place.

Appendix F. X-ray Fluoresence Spectroscopy (XRF)

XRF Theory

X-ray fluorescence spectroscopy works with the same principle of the photo-electric effect as EXAFS. That is, an x-ray is used to liberate inner shell electrons and observe what residual x-rays are given off as a result. The residual x-rays are produced when outer shell electrons collapse to the vacancies left behind. These x-rays are characteristic to the atom and the electron shells of the atom. The analysis produces the identification of the atoms and relative percentages of the atom mass fraction are given. Concentrations in the part per billion can be determined with this technique. However, well known standards or sample spiking with a known quantity of an element are needed for comparison to obtain this level of analysis [Skoog et al., 2007].

The XRF analysis was used to identify any impurities in the $CsSnBr_3$ and CsBr:Sn-1% samples and to identify the relative percentages of the atom species present. The reason for including x-ray fluorescence analysis came from the spectrum seen in Figure 53 where the Sn centered EXAFS scan of CsBr:Sn-1% produced the signature of the Ca K shell electron absporption edge.

In Figure 53 a second absorption edge is found past the Sn L-III edge. Since all absorption edges are fairly well known, a third program called Hephaestus can be used to look up the edge of the second edge in the plot. (There are other published sources as well to find this information.) At 4038-eV this turns out to be the Ca K edge. Fortunately, this data can be subtracted off the end due to Sn EXAFS analysis dependency on the Sn atom spectrum. That is, the x-ray and photoelectron interactions of the Sn are not dependent on any other atom species in the matrix except for their radial positions.
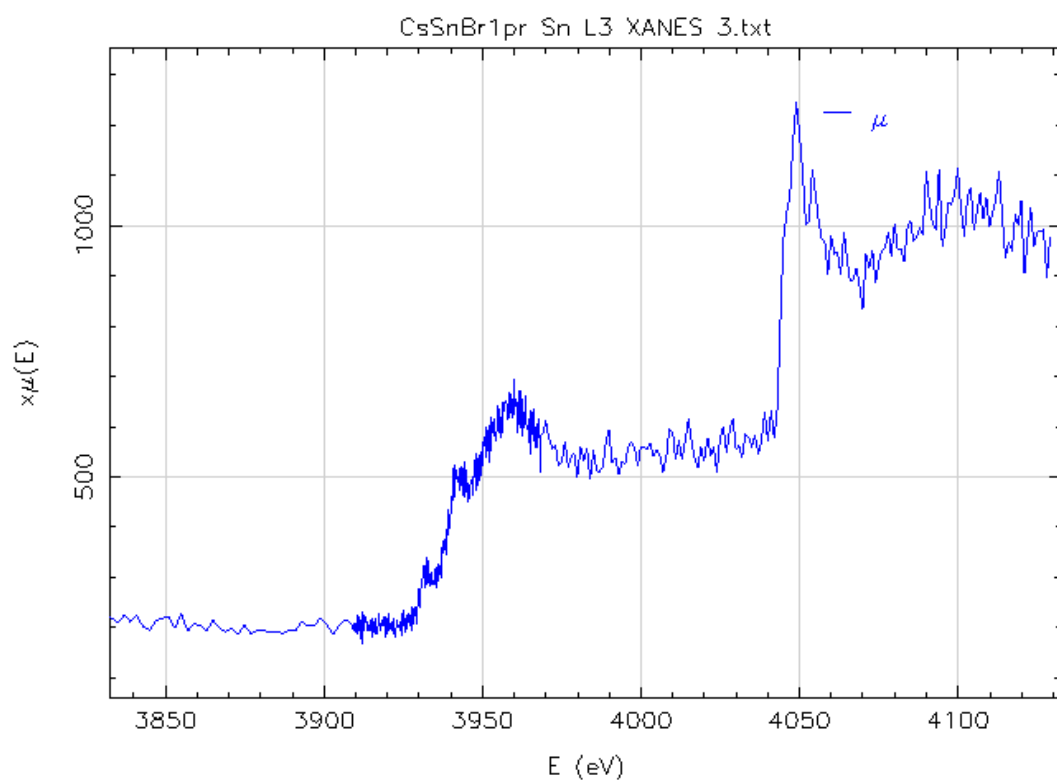
Figure 53. The Ca K absorption edge is the stair-step like structure on the right while the Sn absorption edge used for EXAFS analysis on CsBr:Sn-1% is on the left. Ca is determined to be the element via the signature energy of the Ca K edge which is at 4038-eV.

XRF Equipment

The XRF data were taken on a Horiba XGT-7000V (S/N: F0X0A50J) located in building 470 at AFIT. Samples are mounted on a platform with double sided tape. The tape will cause noise and rhodium spikes in the data. These data can sometimes be filtered out by taking longer measurements of the sample. The noise and background elements will disappear into the background. Elements of low concentration, low Z, or both can be washed out also during long runs. This may be the reason Ca was rarely observed in the spectra.
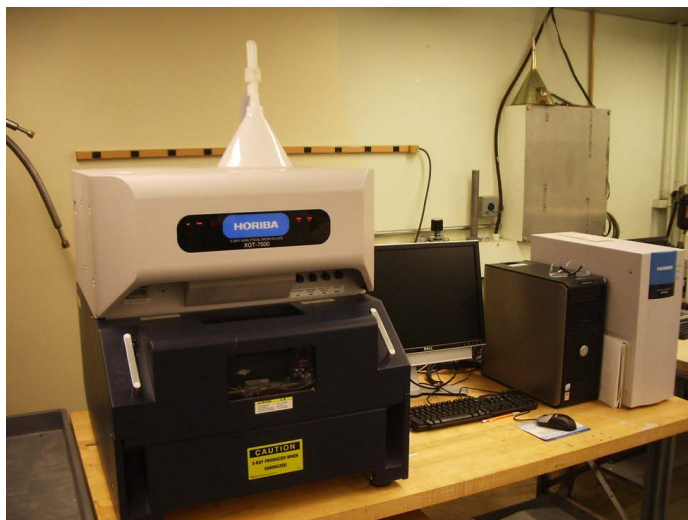
Figure 54. The Horiba XRF machine is shown here. The composition of materials can be analyzed for atoms above Z > 8 [Skoog et al., 2007]. To find quantitative concentrations of a matrix it is necessary to obtain well known standards with compositions close to the material [Skoog et al., 2007].

As with the SEM machine a vacuum is required for the XRF machine to reduce x-ray interaction with the air or other sources of atoms. Both sources of interference can cause false indications of atoms in a sample which may not be present. The x-ray beam energy can be adjusted in order to excite the electron shells of differing Z number atoms. Higher Z atoms require more energy to get K,L and M excitations. The beam size can be either 10 or 100μm. Integration time can also be customized

for desired spectrum intensity results. That is, longer integration times mean higher counts.

The beam scanning can be tailored to perform spot analysis or element scanning. Element scanning was used to find Ca in the crystal samples for this thesis. In most cases, the Ca returns were too low as a mass percentage to be reported. However, the scanning feature would always detect impurities. The scanning feature makes a map of the atomic distribution of a sample.

XRF Results

The XRF results are given in mass as a percentage of all other atomic concentrations detected during a data run. A spectrograph is also produced which shows the atomic electron shell (K, L or M, etc.) and the relative intensity of the indication in counts. Due to broad Gaussian distributions and more abundant molecules, impurities can get washed out of a data run. Figure 55 illustrates these points.
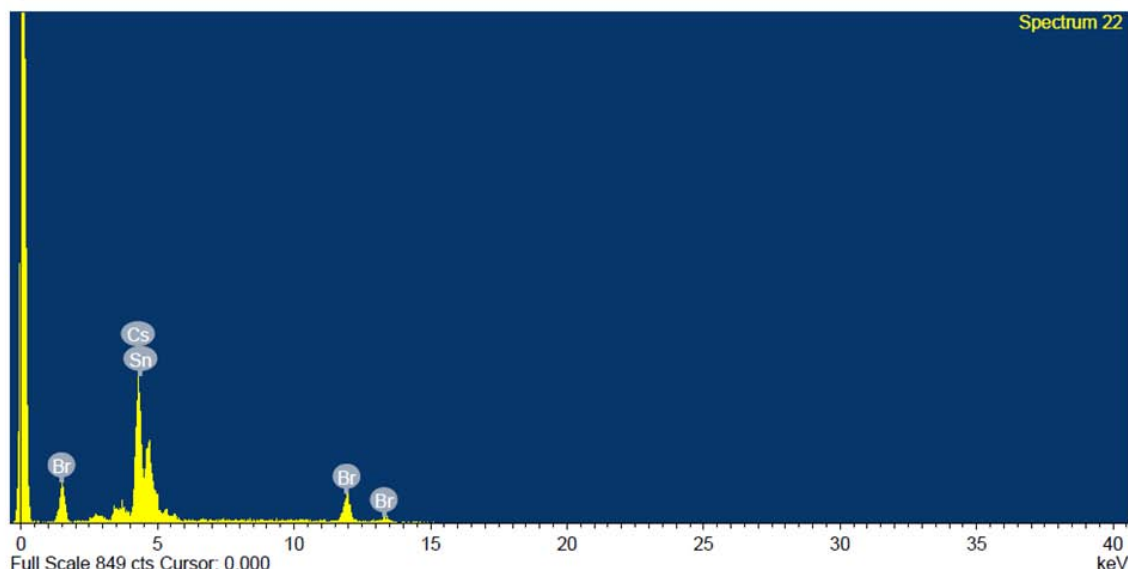
Figure 55. Much like the CL graphs a plot of energy vs. intensity is produced. The elements are identified by their characteristic x-ray fluorescent emissions. This phenomena is the same mechanism by which EXAFS works. The XRF technique is much faster as absorption versus energy dependence is not measured over several energies. An XRF run takes seconds compared to over an hour for an EXAFS run. The Ca is not present in this data sample of CsBr:Sn-1%. The intensity side of the graph is in units of counts. The predominant atoms in the crystal react more often with the x-rays than the impurities. Thus, the Ca signal can be washed out during long runs of data.

Table 8. XRF Results for CsBr:Sn-1%

Element	Mass%
Cs	45.89
Sn	2.66
Br	36.04

The Ca is not present in this data sample of CsBr:Sn-1%. The predominant atoms in the crystal react more often with the x-rays than the impurities. Thus, the Ca signal can be washed out during long runs of data. Oddly enough, Ca was found in the CsSnBr$_3$ sample. Figure 56 below shows the graph for a CsSnBr$_3$ scan.
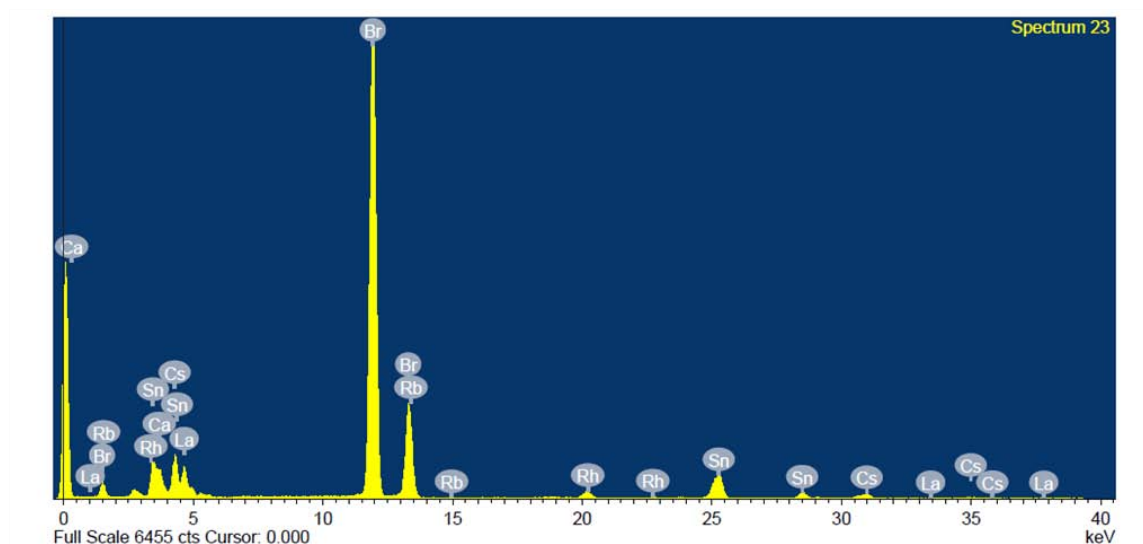
Figure 56. The change in Sn concentration is reflected in Table ??. As Sn becomes more prevalent in the CsBr structure it equals the percentage of Cs. The Ca impurity shows up in this data.

Table 9. XRF Results for CsSnBr$_3$ scan showing calcium impurity

Element	Mass%
Cs	28.73
Sn	25.95
Br	45.32
Ca	2.04

The scanning feature was used on the CsBr:Sn-1% samples to investigate impurities. Calcium would show up in the CsBr:Sn-1% samples on occasion. Figures 57, 58, 59 and 60 show the mapping of a CsBr:Sn-1% against the XRF mount. The Ca shows up very sparsely in Figure 58.
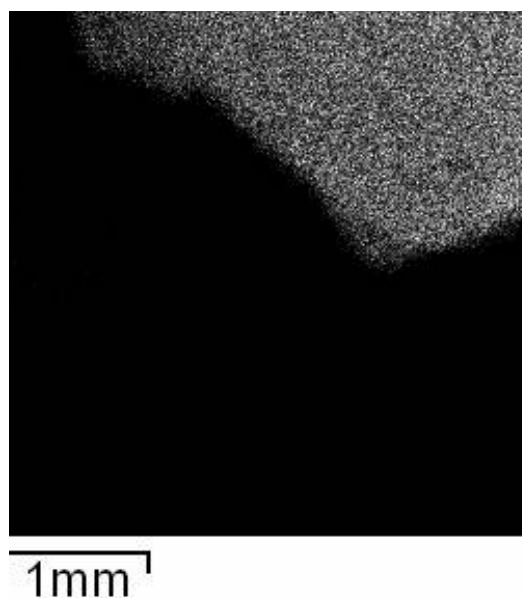
Figure 57. The Cs is very evident throughout the CsBr:Sn-1% crystal in this atom map of the sample. The black part of the image is the background which is tape.
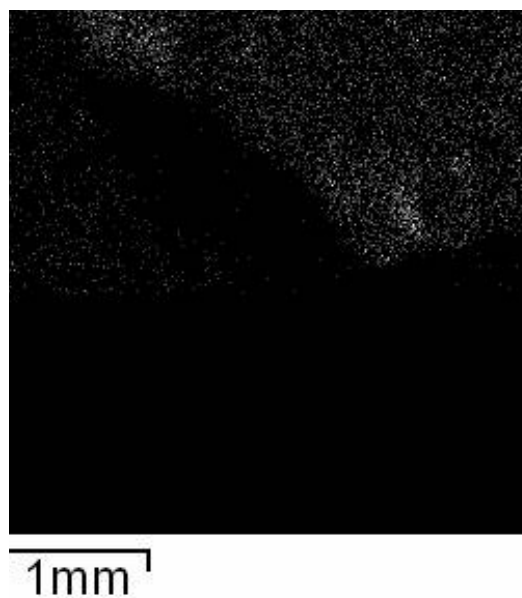
Figure 58. The Ca shows up very rarely in the crystal. The minium concentration to register for XRF is just below 1%. Despite Ca not showing up in the analysis report it is present in the crystal.

1mm
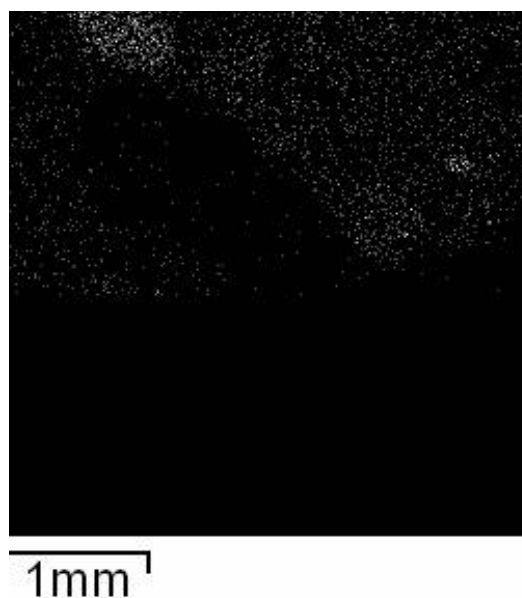
Figure 59. The 1% concentration of Sn is shown evenly distributed throughout the crystal. The response as seen in the image is not as intense as seen for Cs in Figure 57. This is expected as it occurs only 1% of the time in the matrix.

1mm
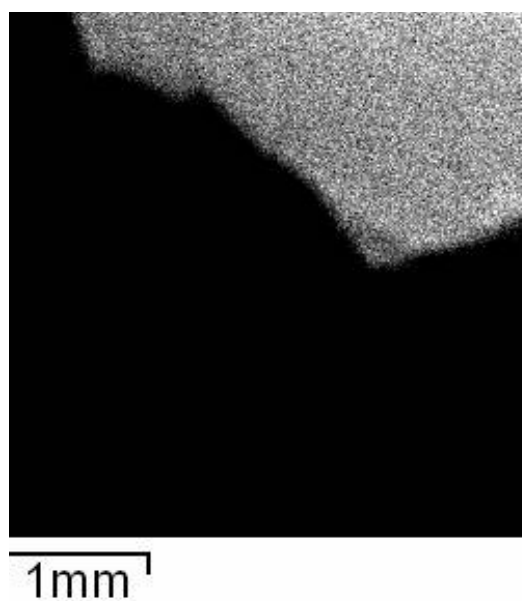
Figure 60. The Br is shown here for completeness. Br is very prevalent in the crystal structure as shown here.

Thus, there is Ca in both CsBr:Sn-1% and CsSnBr$_3$. The effect of the Ca on the luminescence was not researched. The CL data came close to the Savchyn et al. [2007] data. The Savchyn et al. [2007] paper did not investigate the effects of impurities, nor were any impurities discussed.

Appendix G. Other Crystals and Equipment for Scintillation Research

During this research a few more crystals were sent from University of Nebraska, Lincoln as potential crystals for EXAFS and/or luminescence studies. An attempt was made to characterize CsI:CdI$_2$-0.5% as a scintillator material for comparison with CsBr:Sn-1%. Table 10 shows other crystals for possible research. These crystals can be obtained from the ENP department at AFIT.

**Table 10. Other Crystals for Potential Scintillation Research.**

Crystal	General Clearness/Opacity	Potential Scintillator Candidate?
CsI:CdI$_2$-0.5%	Very Clear	Yes
CsI:Pb-1%	Somewhat Clear	Yes
CsI:Sn-1%	Opaque	Maybe

A brief set of experiments were performed on a Hamamatsu MPPC module. The Hamamatsu MPPC module works like a focal plane array (FPA) found in remote sensing systems or a typical digital camera. The FPA is a silicon detector with 100-μm on a side pixels. Each pixel is run in a Geiger counter mode. that is, each pixel is a photon counter. Silicon is primarily a visible to near IR light sensor. The bandwidth and efficiency of the Hamamatsu MPPC module is shown in Figure 61.

The module has the capability to be interfaced with a multi-channel analyzer (MCA). A Compton energy spectrum of an isotope can then be obtained. Unfortunately, when this part of the experiment was attempted the expected Compton energy readings from the module were nonexistent. Due to the lateness of the experiment in the research quarter, it was never repeated.

The Hamamatsu MPPC module was used to measure the light yield of different candidate scintillator materials. The software provided with the module records photon counts per unit time. A threshold of sensitivity can be set between 0.5 and 3.5
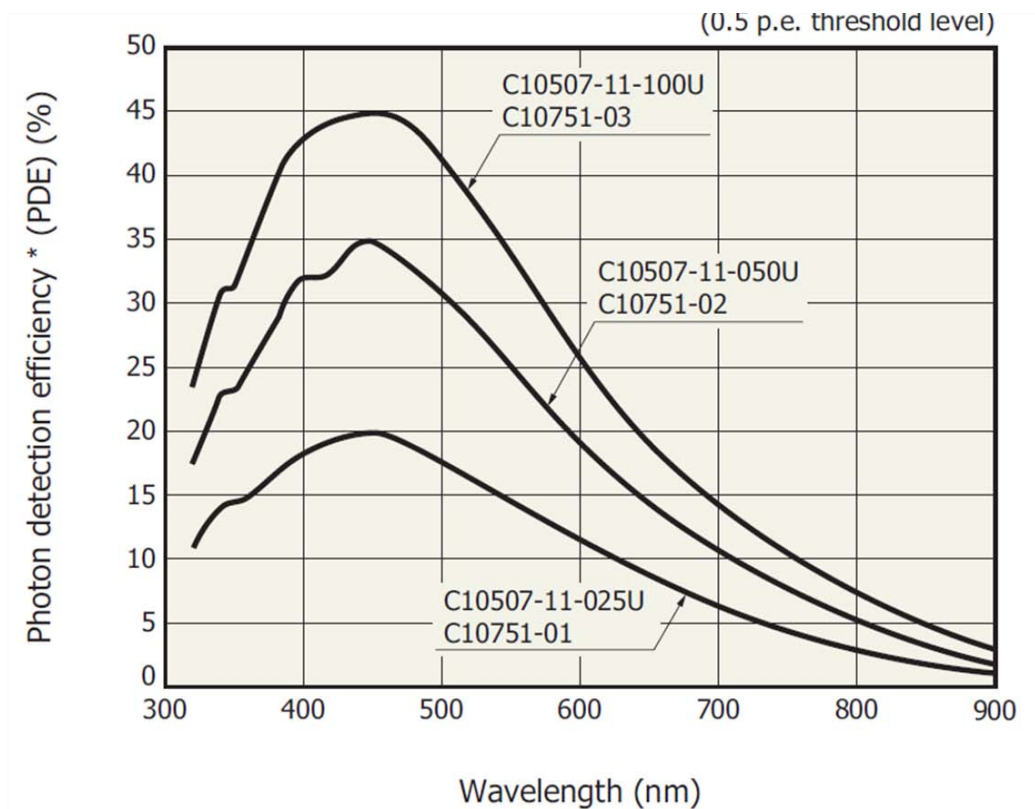
Figure 61. Photon detection efficiency of the Hamamatsu MPPC module as a function of wavelength. The module was used to measure the light yield of different candidate scintillator materials [Division, 2010].

photon events (p.e.). The integration time can be set between 1-ms to 100-ms. The module is very sensitive. The module and material sample were placed in a black electronics project box to block any light. The ^{22}Na and ^{60}Co isotopes listed in Appendix C were used as excitation sources. Figure 62 shows the readout of NaI(Tl) with ^{22}Na as the excitation source.

Figure 63 shows the results of NaI(Tl) with ^{60}Co. This time the source was brought in twice over the experiment. The MPPC can be run indefinitely. Shorter data sets are desirable. The module is creating a data point at every time integration. A point every millisecond, for example, for a couple of seconds is two thousand points. Letting the instrument go for a minute produces a mountain of data.

The CsBr:Sn-1% samples were also tested with the MPPC module. The resulting
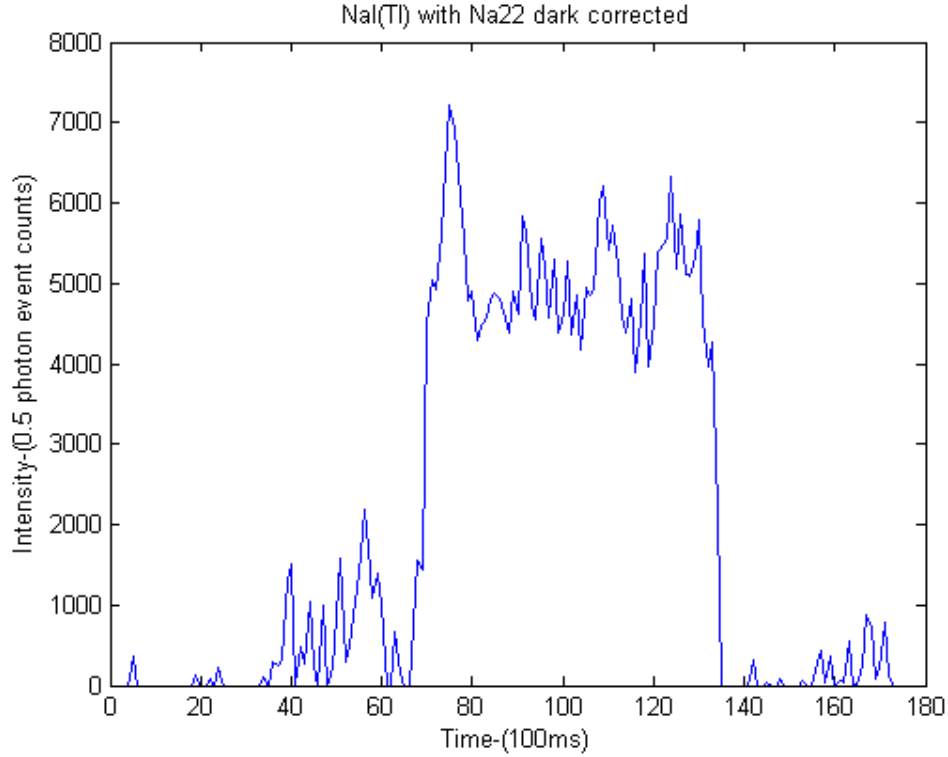
Figure 62. Photon detection efficiency of the Hamamatsu MPPC module as a function of wavelength. The module was used to measure the light yield of different candidate scintillator materials. This graph is intensity vs 100-ms time steps. A ^{22}Na source was moved in by the detector from a great distance. The crown like structure is the effective number of photons per 100-ms. A background, or dark frame, was taken and averaged. The averaged value was then subtracted from each value to give the effective count above the background.

counts are no greater than background noise. ^{60}Co was used in this experiment with comparable settings to the NaI(Tl) experiment in Figure 63. The samples were not optically coupled during the experiments. This was not done to increase speed changing between samples. The CsBr:Sn-1% samples were not properly shaped for optical coupling also.

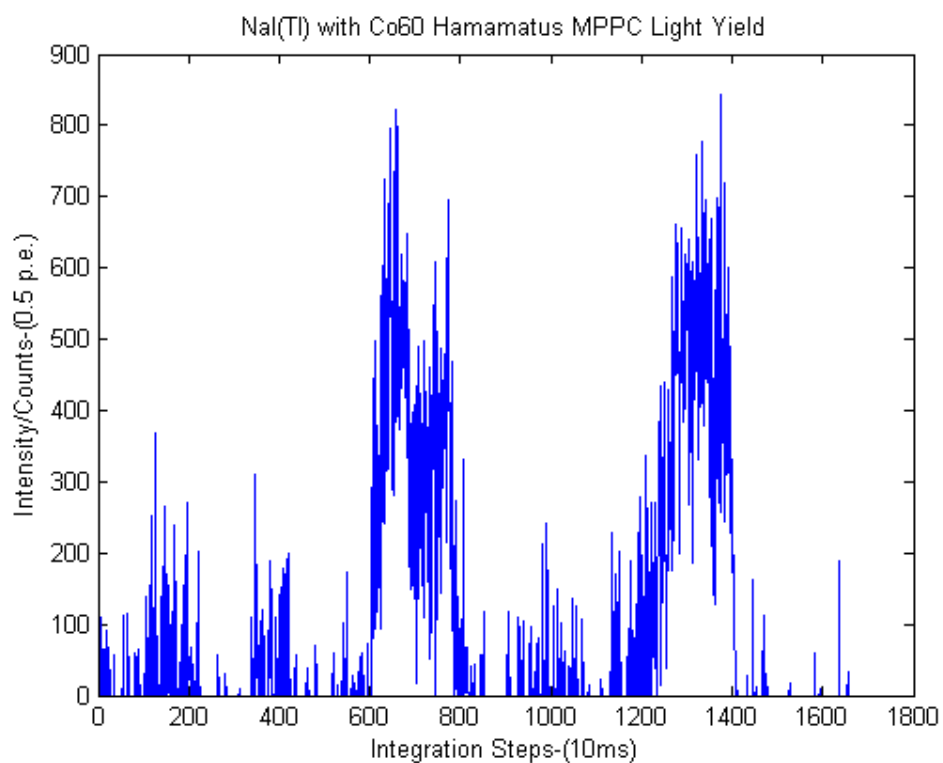**Figure 63.** The same technique used in **Figure 62** was used twice here. ^{60}Co was used giving similar results. There is a difference in integration scale. With the shorter scale, NaI(Tl) still gives a very strong response.
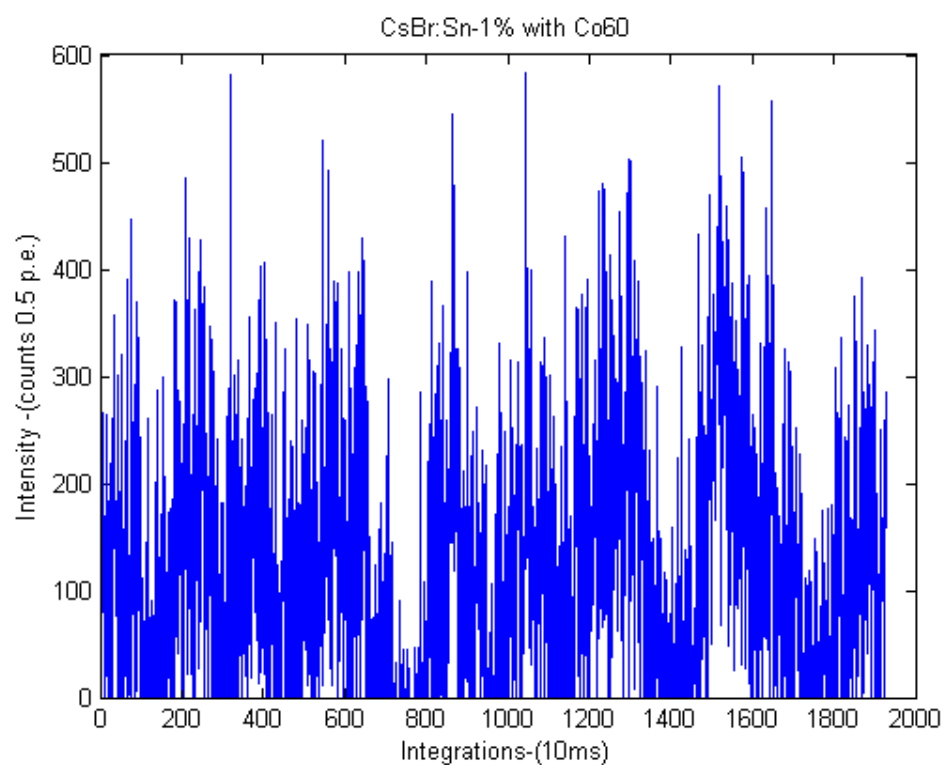
Figure 64. The counts shown here do not vary much farther above the background noise when the ^{60}Co source was brought into close proximity of the target sample.

Appendix H. Table Of Nuclear Isotopes

Table 11. Nuclear Isotopes Used in Photoluminescence Experiment (Activities as of 25 Jan 2010)

Isotope	Activity ($\times 10^5$Bq)	Activity (μCurries)
^{22}Na	20.	54.
^{60}Co	2.0	5.5
^{57}Co	0.41	1.2
^{137}Cs	2.9	7.8
^{109}Cd	3.6	9.8

Most Isotopes in Table 11 did not produce usable data. The CsBr species samples did not produce any useful photoluminescence as described in the results section. The CsI(CdI$_2$) did react with all of the isotopes. The ^{22}Na produced the best results with its considerably higher activity.

Bibliography

Als-Nielsen, Jens, and Des McMorrow. *Elements of Modern X-Ray Physics.* New York, NY: John Wiley and Sons Inc., 2001.

CAMD. "Double Crystal Monochromator (DCM)." `www.camd.lsu.edu/beamlines`, 2008.

Clark, David R. "SSRL Studies Aid Environmental Cleanup at Rocky Flats." `http://www-ssrl.slac.stanford.edu/research/highlights_archive/rocky_flats.pdfl`, 2002.

Cole, M., C. R. A. Catlow, and J. P. Dragun. "EXAFS Studies of Doped-Zr02 Systems." *Journal of Physics and Chemistry of Solids* 51: (1990) 507–513.

Division, Hamamatsu Solid State. "Hamamatsu MPPC Modules." `http://sales.hamamatsu.com/en/products/solid-state-division/si-photodiode-series/mppc-modules/part-c10507-11-025u.php`, 2010.

Hawkes, Peter W, editor. *Advances in Imaging and Electron Physics, Vol 147.* San Diego, CA: Elsevier Inc., 2007.

Kelly, Shelly. "Basics of EXAFS Processing." `http://xafs.org/Tutorials`, 2009a.

———. "Basics of EXAFS Analysis." `http://xafs.org/Tutorials`, 2009b.

Knoll, Glen F. *Radiation Detection and Measurement Third Edition.* Hoboken, NJ: John Wiley and Sons Inc, 2000.

Newville, Matthew. "Fundamentals of EXAFS." `http://xafs.org/Tutorials`, 2004.

NRL. "The Beta Sn (A5) Structure." `cst-www.nrl.navy.mil/lattice/struk/a5.html`, 2004.

Ozawa, Lyuji. *Cathodoluminescence.* New York, NY: Cambridge, 1990.

Ravel, B., and M. Newville. "Athean, Artemis, Hephaestus: data analysis for X-Ray absorption spectroscopy using IFEFFIT." *Journal of Synchrotron Radiation* 12, 4: (2005) 537–541.

Rehr, J. J., and R. C. Albers. "Theoretical Approaches to X-ray Absorption Fine Structure." *Review of Modern Physics* 72: (2000) 621–654.

Savchyn, P. V., S. V. Myagkota, A. S. Voloshinovskii, T. M. Demkiv, and J. R. Datsjuk. "Luminescent Properties of Sn-Based Microcrystals Embedded in a CsBr Matrix." *Radiation Measurement* 42: (2007) 697–700.

Skoog, Douglas A., F. James Holler, and Stanley R. Crouch. *Principles of Instrumental Analysis Sixth Edition.* Belmont, CA: Thomas Brooks, 2007.

Turner, James E. *Atoms, Radioation, and Radiation Protection.* Weinheim, Germany: Wiley VCH, 2007.

Weidner, M., M. Batentschuk, F. Meister, A. Osvet, A. Winnacker, J.-P. Tahon, and P. Leblans. "Luminescence spectroscopy of Eu2+ in CsBr:Eu needle image plates (NIPs),." *Radiation Measurements* 42, 4-5: (2007) 661–664.

Zorenko, Yu V., R.M. Turchak, W. Gryk, and M. Grinberg. "Luminescent Spectroscopy of Eu2+ Centers in CsBr:Eu Single Crystals at 10-550K." *Journal of Luminescence* 106: (2003) 313–320.

REPORT DOCUMENTATION PAGE

1. REPORT DATE (DD-MM-YYYY) 27-03-2010	2. REPORT TYPE Master's Thesis	3. DATES COVERED (From – To) Sep 2009-Mar2010

4. TITLE AND SUBTITLE	5a. CONTRACT NUMBER
The Material Properties of CsSnBr3 and CsBr:Sn-1% and Their Potential as Scintillator Detector Material	5b. GRANT NUMBER
	5c. PROGRAM ELEMENT NUMBER
6. AUTHOR(S) Kleinschmidt, Neal Major, USAF	5d. PROJECT NUMBER
	5e. TASK NUMBER
	5f. WORK UNIT NUMBER

7. PERFORMING ORGANIZATION NAMES(S) AND ADDRESS(S) Air Force Institute of Technology Graduate School of Engineering and Management (AFIT/EN) 2950 Hobson Way WPAFB OH 45433-7765	8. PERFORMING ORGANIZATION REPORT NUMBER AFIT/GNE/ENP/10-M05

9. SPONSORING/MONITORING AGENCY NAME(S) AND ADDRESS(ES) Defense Threat Reduction Agency COL Mark Mattox 1900 Wyoming Blvd SE Kirtland AFB, NM 87117-5669	10. SPONSOR/MONITOR'S ACRONYM(S) DTRA/CSU
	11. SPONSOR/MONITOR'S REPORT NUMBER(S)

12. DISTRIBUTION/AVAILABILITY STATEMENT

APPROVED FOR PUBLIC RELEASE; DISTRIBUTION UNLIMITED

13. SUPPLEMENTARY NOTES

14. ABSTRACT
The search for superior nuclear radiation detection materials is ongoing. Current scintillator materials using Thallium doped Sodium Iodide or Cesium Iodide are the benchmarks for ease of use and quick identification of isotope species. This research aims to explore Cesium Bromide doped with 1% molar tin (CsBr:Sn-1%) and Cesium Tin Bromide (CsSnBr3) as candidate materials for a new scintillator. The techniques of Extended X-Ray Absorption Fine Structure (EXAFS), X-Ray Absorption Near Edge Structure (XANES) and Cathodoluminescence are used to determine the suitability of CsSnBr3 and CsBr:Sn 1% with Sn^{4+} as a potential scintilator materials and explore their crystal and electronic structures. Comparisons with current published work by Savchyn et al. [2007] on CsSnBr3 and CsBr:Sn-1% with Sn^{2+} will be made. Cathodoluminescence shows the CsBr:Sn-1% with Sn^{4+} to luminesce at 2.4-eV and 3.0-eV, green and violet respectively, indicating the strong possibility of using CsBr:Sn-1% as a scintillator.

15. SUBJECT TERMS
EXAFS, XANES, CsBr, cathodoluminescence

16. SECURITY CLASSIFICATION OF:			17. LIMITATION OF ABSTRACT	18. NUMBER OF PAGES	19a. NAME OF RESPONSIBLE PERSON Benjamin R. Kowash, Capt, USAF (ENP)
a. REPORT U	b. ABSTRACT U	c. THIS PAGE U	UU	113	19b. TELEPHONE NUMBER (Include area code) (937)255-3636x4571